

Revisiting the Canonicalization for Fast and Accurate Crystal Tensor Property Prediction

Haowei Hua

Department of Computing
The Hong Kong Polytechnic University

Jingwen Yang

Department of Applied Mathematics
The Hong Kong Polytechnic University

Wanyu Lin*

Department of Computing & Department of Data Science and Artificial Intelligence
The Hong Kong Polytechnic University

Pan Zhou

School of Computing and Information Systems
Singapore Management University

Ming Yang

Department of Applied Physics
Hong Kong Polytechnic University

Yew-Soon Ong

College of Computing and Data Science
Nanyang Technological University

Abstract

Predicting the tensor properties of crystalline materials is a fundamental task in materials science. Unlike single-value property prediction, which is inherently invariant, tensor property prediction requires maintaining $O(3)$ group tensor equivariance. Such equivariance constraint often requires specialized architecture designs to achieve effective predictions, inevitably introducing tremendous computational costs. Canonicalization, a classical technique for geometry, has recently been explored for efficient learning with symmetry. In this work, we revisit the problem of crystal tensor property prediction through the lens of canonicalization. Specifically, we demonstrate how polar decomposition, a simple yet efficient algebraic method, can serve as a form of canonicalization and be leveraged to ensure equivariant tensor property prediction. Building upon this insight, we propose a general $O(3)$ -equivariant framework for fast and accurate crystal tensor property prediction, referred to as *GoeCTP*. By utilizing canonicalization, *GoeCTP* achieves high efficiency without requiring the explicit incorporation of equivariance constraints into the network architecture. Experimental results indicate that *GoeCTP* achieves the best prediction accuracy and runs up to $13\times$ faster compared to existing state-of-the-art methods in benchmarking datasets, underscoring its effectiveness and efficiency.

1 Introduction

The tensor properties of crystalline materials can capture intricate material responses through high-order tensors, with wide-ranging applications in fields such as physics, electronics, and engineering [51]. These tensor properties span various orders, such as dielectric tensor with two orders,

*Corresponding author: wan-yu.lin@polyu.edu.hk

piezoelectric tensor with three orders, and elastic tensor with four orders. Accurate prediction of these tensor properties is critical for novel materials discovery and design with targeted characteristics. Thus far, several works have been dedicated to crystal tensor property prediction. One prominent category involves *ab initio* physical simulation techniques, such as density functional theory (DFT) [35]. These classical simulation techniques can provide acceptable error margin for predicting various material properties. However, they necessitate extensive computational resources due to the complexity of handling large crystals with a vast number of atoms and electrons [51], hindering their applicability in practice.

Alternatively, machine learning (ML) models have been proposed to facilitate the process of crystalline material property prediction. These methods typically leverage high-precision datasets deriving from *ab initio* simulations and utilize crystal graph construction techniques along with graph neural networks (GNNs) [1, 26, 2, 47] or transformers [50, 42, 49, 20, 44]. Most existing methods are designed for scalar property prediction, focusing on achieving $SO(3)$ invariance of the crystal structures. However, these scalar-property methods could not be adapted to predict tensor properties of crystalline materials, which exhibits significantly higher complexity. This complexity arises from the fact that tensor properties describe how crystals respond to external physical fields, such as electric fields or mechanical stress [33, 38, 51]; their modeling necessitates preserving consistency with the crystal’s spatial orientation, exhibiting a unique tensor $O(3)$ equivariance [51].

Therefore, a few recent studies attempt to ensure equivariance through specialized designs of network architectures [28, 25, 11, 46, 34, 51, 53]. These methods generally employ harmonic decomposition to achieve equivariance, where the tensor space is decomposed into the direct sum of irreducible representations of the rotation group. In this regard, numerous computationally intensive operations, such as tensor products and the merging of irreducible representations, are required. These operations incur large amounts of computation overhead, particularly when processing high-order data. *Therefore, providing fast and accurate predictions of tensor properties across various materials is challenging.*

One approach that has show promising results in efficient learning with symmetry across various fields, including point clouds [22], n-body simulation [17], and antibodies generation [29], is the use of “canonicalization”. Specifically, canonicalization maps a geometric data to an invariant representation [27, 6], referred to as the canonical form, and subsequently reconstructs an equivariant output from the canonical form without imposing any architectural constraints on the network. However, to date, it has not been explored for crystal tensor property prediction.

In this work, we revisit the task of crystal tensor property prediction through the lens of canonicalization and introduce a novel canonicalization strategy tailored for this particular setting. Specifically, rather than embedding equivariance directly into model architecture, we propose a simple yet effective canonicalization module, termed R&R. In particular, our canonicalization is instantiated based on polar decomposition, a continuous mapping technique [6] that can provide enhanced robustness. During prediction, the R&R module applies rotations and reflections to transform the input crystal structure into its canonical form. The canonical form is then fed into a property prediction network to obtain the corresponding canonical tensor representation. Simultaneously, the orthogonal matrix derived from the R&R module is utilized to recover the equivariant output via the tensor transformation rule, enabling equivariant tensor property prediction without incurring additional computational overhead. We conducted experiments on dielectric, piezoelectric, and elastic tensor datasets, respectively, showcasing that the proposed method can achieve $O(3)$ -equivariant tensor prediction while maintaining high efficiency. Compared to the previous state-of-the-art work Yan et al. [51], the *GoeCTP* method achieves higher prediction accuracy and runs by up to $13\times$ faster in benchmarking datasets.

2 Background

2.1 Preliminaries

The structure of crystalline materials consists of a periodic arrangement of atoms in 3D space, with a repeating unit called a unit cell. An entire crystal typically can be characterized by describing the parameters of a single unit cell, such as the types and coordinates of the atoms within it, as well as the lattice parameters [49, 45, 16]. General methods for describing crystals can be divided into the Cartesian coordinate system and the fractional coordinate system, as described below.

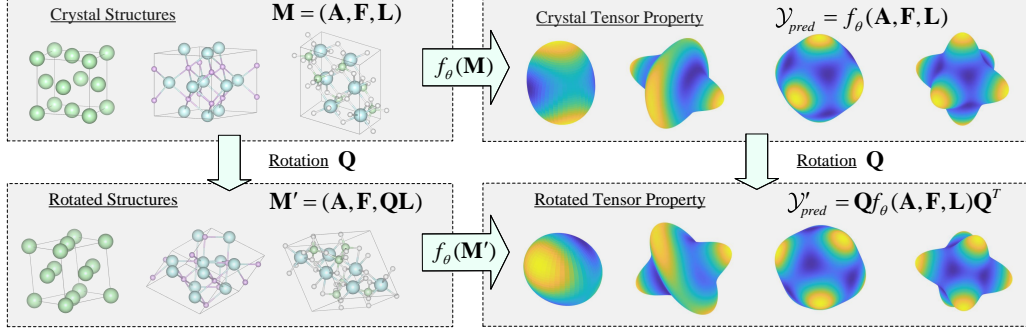


Figure 1: The illustration of $O(3)$ -equivariance for crystal tensor prediction. Some of the visualizations in the figure are generated using the VESTA [30], Yan et al. [51], and VELAS [37].

Cartesian Coordinate System. A crystal can be mathematically represented as $\mathbf{M} = (\mathbf{A}, \mathbf{X}, \mathbf{L})$, where $\mathbf{A} = [\mathbf{a}_1, \mathbf{a}_2, \dots, \mathbf{a}_n]^\top \in \mathbb{R}^{n \times d_a}$ denotes atom features for n atoms within a unit cell. Each $\mathbf{a}_i \in \mathbb{R}^{d_a}$ is a d_a -dimensional feature vector characterizing an individual atom. The matrix $\mathbf{X} = [\mathbf{x}_1, \mathbf{x}_2, \dots, \mathbf{x}_n]^\top \in \mathbb{R}^{n \times 3}$ contains the 3D Cartesian coordinates of n atoms in the unit cell. The lattice matrix $\mathbf{L} = [\mathbf{l}_1, \mathbf{l}_2, \mathbf{l}_3] \in \mathbb{R}^{3 \times 3}$ consists of the lattice vectors \mathbf{l}_1 , \mathbf{l}_2 , and \mathbf{l}_3 , which form the basis of the 3D Euclidean space. A complete crystal is therefore represented as $(\hat{\mathbf{A}}, \hat{\mathbf{X}}) = \{(\hat{\mathbf{a}}_i, \hat{\mathbf{x}}_i) | \hat{\mathbf{x}}_i = \mathbf{x}_i + k_1 \mathbf{l}_1 + k_2 \mathbf{l}_2 + k_3 \mathbf{l}_3, \hat{\mathbf{a}}_i = \mathbf{a}_i, k_1, k_2, k_3 \in \mathbb{Z}, i \in \mathbb{Z}, 1 \leq i \leq n\}$. In this representation, the integers k_i and l_i denote all possible atomic positions in the periodic lattice.

Fractional Coordinate System. Instead of using the standard orthogonal basis, fractional coordinate system utilizes the lattice matrix $\mathbf{L} = [\mathbf{l}_1, \mathbf{l}_2, \mathbf{l}_3] \in \mathbb{R}^{3 \times 3}$ as the basis vectors for atomic positions. With this representation, the position of an atom is given by a fractional coordinate vector denoted as $\mathbf{f}_i = [f_1, f_2, f_3]^\top \in [0, 1)^3$. The corresponding Cartesian coordinate vector can then be expressed as $\mathbf{x}_i = \mathbf{f}_i \mathbf{l}_i$. Therefore, for a crystal \mathbf{M} , it can be represented as $\mathbf{M} = (\mathbf{A}, \mathbf{F}, \mathbf{L})$, where $\mathbf{F} = [\mathbf{f}_1, \dots, \mathbf{f}_n]^\top \in [0, 1)^{n \times 3}$ represents the fractional coordinates of all atoms in the unit cell.

2.2 Problem statement

Crystal Tensor Prediction. The crystal tensor properties prediction is a classic regression task. Its goal is to estimate the high-order tensor property denoted as \mathcal{Y} from the raw crystal data represented as $\mathbf{M} = (\mathbf{A}, \mathbf{F}, \mathbf{L})$. Given that the crystal data \mathbf{M} resides within the input space \mathcal{V} , and the tensor property \mathcal{Y} belongs to the separate output space \mathcal{W} , the objective of crystal tensor prediction is to find a function $f_\theta : \mathcal{V} \rightarrow \mathcal{W}$ that accurately maps input crystal data to the desired tensor property. This is achieved by minimizing the discrepancy between the true property \mathcal{Y} and the predicted property value \mathcal{Y}_{pred} . Therefore, the crystal tensor property prediction task can be mathematically formulated as the following optimization problem:

$$\min_{\theta} \sum_{n=1}^N \|\mathcal{Y}_{pred}^{(n)} - \mathcal{Y}^{(n)}\|^2, \quad \mathcal{Y}_{pred} = f_\theta(\mathbf{A}, \mathbf{F}, \mathbf{L}), \quad (1)$$

where $f_\theta(\cdot)$ represents a tensor prediction model with learnable parameters θ , and the superscript n denotes individual samples in the dataset. In what follows, we will omit superscript n for simplicity. As did in the literature [28, 46, 51], our objective is to estimate high-order tensor properties, including 2-order dielectric tensor (i.e., $\mathcal{Y} \triangleq \epsilon \in \mathbb{R}^{3 \times 3}$), 3-order piezoelectric tensor (i.e., $\mathcal{Y} \triangleq \mathbf{e} \in \mathbb{R}^{3 \times 3 \times 3}$), and 4-order elastic tensor (i.e., $\mathcal{Y} \triangleq \mathbf{C} \in \mathbb{R}^{3 \times 3 \times 3 \times 3}$), respectively.

$O(3)$ group. The $O(3)$ group is an orthogonal group, consisting of rotations and reflections. The elements $g \in O(3)$ act on vectors or tensors in \mathcal{V}, \mathcal{W} through their respective group representations, $\rho_V : O(3) \rightarrow GL(\mathcal{V})$ and $\rho_W : O(3) \rightarrow GL(\mathcal{W})$, where $GL(\mathcal{V})$ and $GL(\mathcal{W})$ are the space of invertible linear maps $\mathcal{V} \rightarrow \mathcal{V}$ and $\mathcal{W} \rightarrow \mathcal{W}$, respectively. Specifically, the action of an element $g \in O(3)$ on crystal data \mathbf{M} is defined as: $g \cdot \mathbf{M} = \rho_V(g)\mathbf{M} = (\mathbf{A}, \mathbf{F}, \mathbf{QL})$. For dielectric

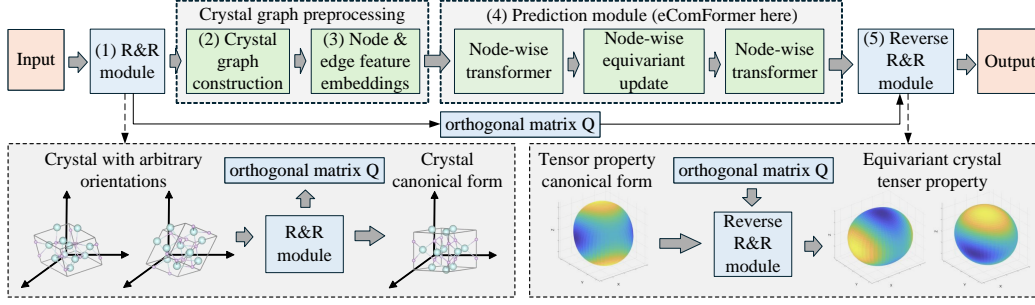


Figure 2: The Illustration of *GoeCTP*. To begin with, **(1)** the R&R module rotates and reflects the input crystal structure, which may have an arbitrary orientation, to the canonical form of this crystal. Next, **(2)** Crystal Graph Construction module organizes the adjusted input into a crystal graph, followed by **(3)** the Node & Edge Feature Embedding module, which encodes the features of the crystal graph. Subsequently, **(4)** the Prediction module leverages these embedded features to predict the canonical form of tensor properties corresponding to the canonical form of input crystal. Finally, **(5)** the Reverse R&R module applies the orthogonal matrix \mathbf{Q} , obtained from the R&R module, to ensure the equivariance of the output tensor properties.

tensor property \mathcal{Y} , the action of g is given by: $g \cdot \mathcal{Y} = \rho_{\mathcal{W}}(g)\mathcal{Y} = \mathbf{Q}\mathcal{Y}\mathbf{Q}^\top$, where \mathbf{Q} is a 3×3 orthogonal matrix (for additional details regarding the transformation of tensor properties, please refer to Appendix A.8).

O(3)-Equivariance for Crystal Tensor Prediction. In the crystal tensor properties prediction task, due to the difference between $\rho_{\mathcal{V}}(g)$ and $\rho_{\mathcal{W}}(g)$, the requirements for $O(3)$ equivariance typically differ from the $O(3)$ -equivariance defined in the general molecular studies [13, 48, 52, 40]. Specifically, taking the dielectric tensor as an example where $\mathcal{Y}_{label} \triangleq \boldsymbol{\epsilon} \in \mathbb{R}^{3 \times 3}$, for a tensor prediction model $f_\theta(\cdot)$ in Eq. 1, if it is $O(3)$ equivariant, it must satisfy the following equality formulated as:

$$f_\theta(\mathbf{A}, \mathbf{F}, \mathbf{Q}\mathbf{L}) = \mathbf{Q}f_\theta(\mathbf{A}, \mathbf{F}, \mathbf{L})\mathbf{Q}^\top, \quad (2)$$

where $\mathbf{Q} \in \mathbb{R}^{n \times n}$ is an arbitrary orthogonal matrix [51]. For clarity, an illustration of $O(3)$ -equivariance for crystal tensor prediction is shown in Fig. 1 (for more equivariance details, see Appendix A.8).

3 Methodology

In this section, we will first provide the motivation driving our new framework. We then reformulate the $O(3)$ equivariant tensor prediction task from the perspective of canonicalization. Building upon this foundational perspective, we demonstrate how polar decomposition can be employed as a canonicalization strategy and effectively applied to solve tensor prediction tasks with both effectiveness and efficiency.

3.1 The Motivation of Our Framework

To enforce $O(3)$ equivariance, as described in Eq. 2, existing crystal tensor prediction methods typically employ specialized network architectures based on harmonic decomposition, resulting in substantial computational overhead. For example, existing work gather the rotational information from the neighboring nodes to the central node i through the following computation formulated [51]:

$$\mathbf{f}_{i,\lambda}^l = \frac{1}{|\mathcal{N}_i|} \sum_{j \in \mathcal{N}_i} \mathbf{TP}_\lambda(\mathbf{f}_j^{l'}, \mathbf{Y}_\lambda(\hat{\mathbf{e}}_{ji})), \quad (3)$$

where \mathbf{f}_i^l is node i 's features, $|\mathcal{N}_i|$ is the number of neighbors of node i , \mathbf{TP}_λ refers to tensor product layers with rotation order λ [7], and $\mathbf{Y}_\lambda(\hat{\mathbf{e}}_{ji})$ represents the equivariant edge feature embedding,

which is embedded by the corresponding spherical harmonics. To achieve $O(3)$ equivariance of the model and ensure high prediction accuracy for high-order tensor prediction tasks, such as elastic tensor prediction, the rotation order λ is set to 3 [51], i.e., $\mathbf{Y}_3(\hat{\mathbf{e}}_{ji}) \in \mathbb{R}^7$. In contrast, for lower-order tensor prediction tasks, setting λ to 1 is sufficient to achieve the model’s $O(3)$ equivariance, i.e., $\mathbf{Y}_1(\hat{\mathbf{e}}_{ji}) \in \mathbb{R}^3$. Compared to lower-order tensor prediction, the dimension of $\mathbf{Y}_\lambda(\hat{\mathbf{e}}_{ji})$ nearly doubles for high-order tensor predictions, leading to a significant increase in computational complexity. Consequently, this model architecture introduces tremendous computational costs for tensor property predictions. If we can achieve the model’s $O(3)$ equivariance and maintain the model performance for higher-order tensors with a lower value of λ , e.g., $\lambda = 1$, or even without relying on harmonic decomposition, computational costs could be drastically reduced. Inspired by the recent exploration of using canonicalization in efficient learning with symmetry, we aim to propose a principled approach based on canonicalization to enable $O(3)$ -equivariant tensor predictions for crystal materials.

3.2 $O(3)$ Equivariant Tensor Prediction from the Perspective of Canonicalization

To mathematically describe $O(3)$ -equivariant tensor prediction from the perspective of canonicalization, we first introduce and extend several fundamental concepts derived from canonicalization techniques [27, 17, 6].

Definition 3.1. (*Orbit.*) The orbit of a crystal \mathbf{M} is defined as $\text{Orbit}(\mathbf{M}) = \{g \cdot \mathbf{M} \mid g \in O(3)\}$.

In the context of crystal tensor prediction, all configurations of a crystal (i.e. a crystal with different orientations) in the space fall into the same orbit under the $O(3)$ group transformation. Specifically, for any two crystal configurations denoted as \mathbf{M}_1 and \mathbf{M}_2 within the same orbit, there exists a rotation or reflection $g \in O(3)$ such that $\mathbf{M}_1 = g \cdot \mathbf{M}_2$. Likewise, the tensor properties of the crystal also exhibit an orbit, i.e. $\text{Orbit}(\mathcal{Y}) = \{g \cdot \mathcal{Y} \mid g \in O(3)\}$. All configurations of a crystal within an orbit could be transformed into one another through group transformations. Consequently, we can select a specific configuration from the orbit to serve as a canonical representative (referred to as the *canonical form*) that effectively characterizes the entire orbit. The formal process is outlined in the following definition.

Definition 3.2. (*Orbit Canonicalization.*) A function denoted as $C_{\mathbf{M}} : \mathcal{V} \rightarrow \mathcal{V}$ is defined as an orbit canonicalization, if $\forall \mathbf{M}_1 \in \text{Orbit}(\mathbf{M})$ and $\exists \mathbf{M}_0 \in \text{Orbit}(\mathbf{M})$, such that $C_{\mathbf{M}}(\mathbf{M}_1) = \mathbf{M}_0$, where \mathbf{M}_0 is the canonical form of the orbit.

Orbit canonicalization enables the transformation of a crystal with arbitrary orientations in the space into one with a specific, well-defined orientation. Since the output of orbit canonicalization can always be mapped to the invariant canonical form, it follows that $C_{\mathbf{M}}(\cdot)$ itself is $O(3)$ -invariant. Therefore, for any prediction function $f_\theta(\cdot)$, it holds that $f_\theta(C_{\mathbf{M}}(\cdot))$ remains $O(3)$ -invariant (See the proof in Appendix A.1).

Although an $O(3)$ -invariant prediction function has been established via orbit canonicalization, the complete process of equivariant prediction requires specific group transformations that map all crystal configurations within the orbit to their canonical form. To address this requirement, we introduce the concept of rigid registration. Rigid registration is a fundamental concept in fields such as computer vision and computational geometry [41]. It aims to find a transformation that matches the position and orientation of one object with the corresponding position and orientation of another object. This concept can be naturally adapted to the crystal, as follows.

Definition 3.3. (*Rigid Registration.*) A function $R_{\mathbf{M}} : \mathcal{V} \times \mathcal{V} \rightarrow O(3)$ is a rigid registration if $\forall \mathbf{M}_1, \mathbf{M}_2 \in \text{Orbit}(\mathbf{M})$, $R_{\mathbf{M}}(\mathbf{M}_1, \mathbf{M}_2) = g$, such that $\mathbf{M}_1 = g \cdot \mathbf{M}_2$.

Using Definition 3.3, we can identify a transformation that matches two configurations of a crystal. Specifically, this allows us to find specific group transformations that map all crystal configurations within the orbit to their canonical form. By leveraging Definition 3.2 and Definition 3.3 together, we derive a view for performing $O(3)$ -equivariant tensor prediction through canonicalization, as described below.

Proposition 3.4. (*$O(3)$ -Equivariant Tensor Prediction from the Perspective of Canonicalization.*) Given an arbitrary tensor prediction function $f(\mathbf{M}) : \mathcal{V} \rightarrow \mathcal{W}$, we can define a new function formulated as $h(\mathbf{M}) = R_{\mathbf{M}}(\mathbf{M}, C_{\mathbf{M}}(\mathbf{M})) \cdot f(C_{\mathbf{M}}(\mathbf{M}))$, such that $h(\mathbf{M})$ is $O(3)$ -equivariant for tensor prediction.

The proof of Proposition 3.4 is provided in Appendix A.6. Specifically, in this unified view of $O(3)$ equivariant tensor prediction, we leverage rigid registration, as defined in Definition 3.3, to find specific group transformations that map crystal configurations within the orbit to their canonical form. This canonical form is determined through orbit canonicalization, as described in Definition 3.2. Subsequently, we can directly apply these transformations to the network’s output, thereby effectively achieving the $O(3)$ equivariance. That is, under this perspective, there are no specific requirements or special treatments needed for the network design, as the $O(3)$ transformations applied to the crystal can be externally determined and simultaneously applied directly to the output. Building upon Proposition 3.4, the key challenge in achieving $O(3)$ -equivariant tensor prediction lies in identifying the appropriate orbit canonicalization and rigid registration functions.

3.3 Our Proposed Framework: *GoeCTP*

In what follows, we demonstrate that polar decomposition can effectively serve as both orbit canonicalization and rigid registration functions for crystal tensor prediction. Building on this foundation, we will first introduce the core rotation and reflection (R&R) module of the proposed *GoeCTP*, which is to obtain the canonical form for a crystal with arbitrary spatial orientations using polar decomposition. Then, we will describe how the input crystal data is processed and introduce the property prediction network of *GoeCTP*. Finally, we will explain how proposed *GoeCTP* achieves equivariant tensor predictions. An overview of the *GoeCTP* framework is illustrated in Fig. 2.

Theorem 3.5. (*Polar Decomposition [9, 12, 16].*) An invertible matrix $\mathbf{L} \in \mathbb{R}^{3 \times 3}$ can be uniquely decomposed into $\mathbf{L} = \mathbf{QH}$, where $\mathbf{Q} \in \mathbb{R}^{3 \times 3}$ is an orthogonal matrix, $\mathbf{H} \in \mathbb{R}^{3 \times 3}$ is a Hermitian positive semi-definite matrix.

In the fractional coordinate system, the $O(3)$ group transformations applied to a crystal affect only the lattice matrix \mathbf{L} , while fractional coordinates remain invariant, making it convenient for rotating the crystal configuration to the canonical form. Therefore, throughout this work, we adopt the fractional coordinate system to represent the crystal represented as $\mathbf{M} = (\mathbf{A}, \mathbf{F}, \mathbf{L})$. Then building on Theorem 3.5, we can define both orbit canonicalization and rigid registration functions for crystal tensor prediction as follows.

Proposition 3.6. (*Orbit Canonicalization and Rigid Registration for Crystal Tensor Prediction.*) By performing polar decomposition on the lattice matrix $\mathbf{L} = \mathbf{QH}$ of a crystal \mathbf{M} , we can define functions $f_{p1}(\mathbf{M}) = (\mathbf{A}, \mathbf{F}, \mathbf{H})$ and $f_{p2}(\mathbf{M}, f_{p1}(\mathbf{M})) = \mathbf{Q}$, where $f_{p1}(\cdot)$ and $f_{p2}(\cdot)$ correspond to performing polar decomposition on the lattice matrix. In this perspective, $f_{p1}(\cdot)$ serves as the orbit canonicalization function, while $f_{p2}(\cdot)$ serves as the rigid registration function. The crystal configuration $\mathbf{M}_0 = (\mathbf{A}, \mathbf{F}, \mathbf{H})$ is thus identified as the canonical form.

The detailed proof of Proposition 3.6 is provided in Appendix A.7. Specifically, since the polar decomposition of a lattice matrix always exists and it is unique, any orthogonal matrix acting on the lattice matrix can be separated through polar decomposition, yielding a unique \mathbf{H} . Thus, \mathbf{H} can serve as the canonical form. Moreover, the rationale of using polar decomposition is that it is a continuous canonicalization, which can provide improved robustness [6]. For clarity, we provide details on this continuity in Appendix A.14, and further discussions on constructing alternative canonical forms based on polar decomposition in Appendix A.15, respectively. Building upon Proposition 3.6, we utilize polar decomposition to construct the proposed *GoeCTP* model.

R&R Module. The primary function of the R&R Module is to rotate the crystal configuration to its canonical form and obtain the corresponding transformation. Therefore, based on Proposition 3.6, the R&R Module directly applies polar decomposition to the lattice matrix \mathbf{L} to construct the rigid registration and the orbit canonicalization. Formally, the R&R Module can be expressed as:

$$f_{p1}(\mathbf{M}) = (\mathbf{A}, \mathbf{F}, \mathbf{H}), f_{p2}(\mathbf{M}, f_{p1}(\mathbf{M})) = \mathbf{Q}, \quad (4)$$

where $f_{p1}(\cdot)$ is the orbit canonicalization function, while $f_{p2}(\cdot)$ is the rigid registration function. As shown in Fig. 2, the crystal configuration $(\mathbf{A}, \mathbf{F}, \mathbf{H})$ derived from orbit canonicalization is passed to the subsequent crystal graph construction module for further processing. The orthogonal matrix \mathbf{Q} obtained during this decomposition is passed to the reverse R&R module, ensuring the equivariant transformation of the output tensor properties. Our proposed R&R module based on polar decomposition allows the input crystal data to be transformed into the canonical form that is invariant under $O(3)$ space group transformations. With this particular module, the equivariance can

be captured, meaning that the subsequent components of *GoeCTP* are no longer required to account for equivariance.

Crystal Graph Construction. To enable networks to handle such infinite crystal structures ($\mathbf{A}, \mathbf{F}, \mathbf{H}$), it is typically necessary to employ graph construction methods that represent the interactions between infinite crystal structures and atoms using finite graph data. Here, we use the crystal graph construction from Yan et al. [50, 51] to describe the structure and relationships within crystals. A detailed explanation of the crystal graph construction can be found in Appendix A.2. Upon construction, the edge features are denoted as e_{ij} , while the node features, representing atomic properties, are denoted as a_i .

Node and Edge Feature Embedding. Building on previous work [47, 51, 50], node features a_i are embedded into a 92-dimensional CGCNN feature vector f_i . Edge features e_{ij} are decomposed into their magnitude $\|e_{ij}\|_2$ and a normalized direction vector \hat{e}_{ij} . The magnitude is further mapped to a term similar to potential energy, $-c/\|e_{ij}\|_2$, through the application of a radial basis function (RBF) kernel for encoding [21]. Subsequently, e_{ij} are embedded into feature vector f_{ij}^e .

Prediction Module. Since the R&R module is responsible for preserving equivariance, any predictive network can serve as the Prediction module, such as those proposed by Yan et al. [50], Taniai et al. [42], Yan et al. [49], Lee et al. [20], Wang et al. [44], among others. For better performance, we select eComFormer [50], which has demonstrated excellent performance in single-value property prediction tasks, as our Prediction module. A detailed explanation of eComFormer can be found in Appendix A.2. Once processed through the stacked layers of eComFormer, the node features are aggregated to generate the crystal’s global features as follows: $\mathbf{G}^{\text{final}} = \frac{1}{n} \sum_{1 \leq i \leq n} \mathbf{f}_i^{\text{final}}$.

Reverse R&R Module. The primary function of the Reverse R&R module is to generate the equivariant tensor property predictions based on the crystal global features from the Prediction module. First, the Reverse R&R module transforms $\mathbf{G}^{\text{final}}$ into a tensor output, as follows:

$$\varepsilon = f_{MLP}(\mathbf{G}^{\text{final}}) \quad (5)$$

$$\varepsilon^{\text{final}} = f_{rp}(\varepsilon, \mathbf{Q}), \quad (6)$$

where $f_{MLP}(\cdot)$ represents a multilayer perceptron (MLP) and the operation reshaping dimension. Next, $f_{rp}(\cdot)$ utilizes the orthogonal matrix \mathbf{Q} obtained from the R&R Module to convert the tensor output ε into its final equivariant form denoted as $\varepsilon^{\text{final}}$.

This conversion $f_{rp}(\cdot)$ for predicting the dielectric tensor can be expressed by:

$$\varepsilon^{\text{final}} = \mathbf{Q}\varepsilon\mathbf{Q}^T. \quad (7)$$

For predicting the higher-order piezoelectric and elastic tensor, the conversion process becomes more complex, see Appendix A.8 for more details.

4 Experiments

4.1 Experimental setup

Datasets. In this work, we evaluate the performance of *GoeCTP* on three key tensor property prediction tasks: the second-order dielectric tensor, the third-order piezoelectric tensor, and the fourth-order elastic tensor, respectively. Further details of the dataset and experimental setup can be found in Appendix A.10.

Baseline Methods. We selected several state-of-the-art methods in the field of crystal tensor property prediction, i.e. MEGNET [1, 31], EGTNN [53], and GMTNet [51], as baseline methods.

Evaluation Metrics. We followed the evaluation metrics defined by Yan et al. [51] to assess the performance of the methods. The following metrics were employed: (1) **Frobenius norm (Fnorm)** is used to measure the difference between the predicted tensor and the label tensor, which is the square root of the sum of the squares of all elements in a tensor. Fnorm is widely used in various regression tasks. (2) **Error within threshold (EwT)** is determined by the ratio of the Fnorm between the predicted tensor and the ground truth tensor to the Fnorm of the ground truth tensor. This ratio can be expressed as $\|y_{pred} - y_{label}\|_F / \|y_{label}\|_F$, where $\|\cdot\|_F$ is Fnorm, and y_{label} and y_{pred} represent the ground truth and predicted values, respectively. For instance, EwT 25% indicates that the proportion

of predicted samples with this ratio is below 25%. Higher values of EwT signify better prediction quality. In our experiments, we utilized several thresholds for EwT: EwT 25%, EwT 10%, and EwT 5%.

4.2 Experimental Results

Predicting Dielectric Tensors. The performance of various models in predicting the dielectric tensor is summarized in Table 1. While *GoeCTP* and GMTNet show close results in terms of Fnorm and EwT 25%, *GoeCTP* demonstrates higher values for EwT 10% and EwT 5%, with an improvement of 5% in EwT 5% compared to GMTNet. This indicates that *GoeCTP* delivers higher-quality predictions compared to GMTNet. Furthermore, as *GoeCTP* is designed to be a flexible framework, we also evaluated its combination with other models, such as iComFormer [50] and CrystalFormer [42]. Detailed results of these combinations are provided in Appendix A.11. In addition to these experimental results, we further investigate the impact of different canonical forms on tensor property prediction in crystalline materials. Detailed analyses can be found in Appendix A.16.

	MEGNET	ETGNN	GMTNet	GoeCTP (Ours)
Fnorm ↓	3.71	3.40	3.28	3.23
EwT 25% ↑	75.8%	82.6%	83.3%	83.2%
EwT 10% ↑	38.9%	49.1%	56.0%	56.8%
EwT 5% ↑	18.0%	25.3%	30.5%	35.5%

Table 1: Comparison of performance metrics between MEGNET, ETGNN, GMTNet, and GoeCTP on the dielectric dataset.

Predicting Piezoelectric Tensors. The experimental results for the elastic tensor dataset are shown in Table 2. Similar to the experimental results on the dielectric tensors dataset, it achieves optimal results on all evaluation metrics. Further details on the results of *GoeCTP*’s combination with other models can be found in Appendix A.11.

	MEGNET	ETGNN	GMTNet	GoeCTP (Ours)
Fnorm ↓	0.504	0.515	0.450	0.431
EwT 25% ↑	39.3%	36.3%	45.5%	46.9%
EwT 10% ↑	27.1%	20.5%	38.1%	42.9%
EwT 5% ↑	11.4%	13.0%	34.3%	39.7%

Table 2: Comparison of performance metrics between MEGNET, ETGNN, GMTNet, and GoeCTP on the piezoelectric dataset.

Predicting Elastic Tensors. Experimental results on the elastic tensor dataset are presented in Table 3. *GoeCTP* demonstrated outstanding performance in predicting higher-order, complex tensors, outperforming all baseline methods across every evaluation metric. Notably, it achieved the lowest Fnorm of 107.11 and improved all EwT metrics by an average of 6% compared to GMTNet, emphasizing its general applicability in predicting diverse tensor properties in materials science. Further details on the results of *GoeCTP*’s combination with other models can be found in Appendix A.11.

	MEGNET	ETGNN	GMTNet	GoeCTP (Ours)
Fnorm ↓	143.86	123.64	117.62	107.11
EwT 25% ↑	23.6%	32.0%	36.0%	42.5%
EwT 10% ↑	3.0%	3.8%	7.6%	15.3%
EwT 5% ↑	0.5%	0.5%	2.0%	7.2%

Table 3: Comparison of performance metrics between MEGNET, ETGNN, GMTNet, and GoeCTP on the elastic dataset.

Verifying the $O(3)$ Equivariance. To evaluate the effectiveness of *GoeCTP*, we conducted experiments to verify the $O(3)$ equivariance of tensor properties. Specifically, after training *GoeCTP*, we extracted its Prediction module (i.e., eComFormer) for comparative testing on two different test sets (original test set and augmented test set). All crystals in the original test set were adjusted to the

	eCom. (ori. data)	eCom. (aug. data)	GoeCTP (Ours) (ori. data)	GoeCTP (Ours) (aug. data)
Dielectric: Fnorm ↓	3.23	4.71	3.23	3.23
Total Time (s) ↓	26.03	26.01	26.23	26.18
Piezoelectric: Fnorm ↓	0.431	0.527	0.431	0.431
Total Time (s) ↓	37.83	37.23	38.01	37.71
Elastic: Fnorm ↓	107.11	138.45	107.11	107.11
Total Time (s) ↓	83.26	83.02	90.10	89.60

Table 4: Ablation study for verifying the $O(3)$ equivariance with dielectric, piezoelectric, and elastic dataset. After training *GoeCTP*, we extracted its Prediction module (i.e., eComFormer) for comparative testing on two different test sets

canonical form, while the augmented test set was generated by applying arbitrary $O(3)$ group transformations to all crystals in the original test set. The method for generating the corresponding orthogonal matrices is from Heiberger [10]. We then evaluated both the Prediction module (eComFormer) and *GoeCTP* on these two datasets and compared the performance metrics.

The results on the three tensor datasets are shown in Table 4, *GoeCTP* performed equally well on the augmented test set as on the original test set in all tensor datasets, indicating that it maintains strong $O(3)$ equivariance for tensor properties. In contrast, the performance of the eComFormer method significantly declined on the augmented test set, with Fnorm decreasing by nearly 45% in dielectric tensor dataset, nearly 22% in piezoelectric tensor dataset, and nearly 29% in elastic tensor dataset, demonstrating that it does not meet the $O(3)$ equivariance requirements for tensor properties.

Additionally, runtime comparisons between *GoeCTP* and eComFormer on the test set revealed that *GoeCTP* did not result in a significant increase in runtime. This demonstrates that when integrated into single-value property prediction networks, *GoeCTP* incurs almost no additional computational cost, enhancing its practicality while maintaining efficiency.

Efficiency. The results presented in Table 5, Table 6, and Table 7 illustrate the running times for *GoeCTP* and baseline methods. On the dielectric dataset, *GoeCTP* completed the entire training process with only 38.2% of the time spent compared to GMTNet. On the piezoelectric dataset, *GoeCTP* completed the entire training process with only 16.3% of the time spent compared to GMTNet. On the elastic dataset, *GoeCTP* required less than 7.0% of the time spent by GMTNet to complete the entire training process.

To achieve $O(3)$ equivariance for tensor properties, GMTNet’s network architecture relies on irreducible representations and tensor operations, which considerably reduce computational efficiency, especially for higher-order tensor property (elastic tensor) prediction tasks where the time cost of GMTNet increases sharply. In contrast, *GoeCTP* requires no special architectural design for tensor property prediction tasks; it predicts tensor properties of varying orders using only a MLP at the network’s output, ensuring both efficiency and scalability across different tensor orders.

5 Concluding Remarks

In this work, we revisit crystal tensor property prediction through the lens of canonicalization. Built upon the notion of canonicalization, we proposed a novel $O(3)$ -equivariant framework *GoeCTP* for fast and accurate crystal tensor prediction. Benefiting from the canonicalization mechanism, *GoeCTP*

	MEGNET	ETGNN	GMTNet	GoeCTP (Ours)
Total Time (s) ↓	663	1325	1611	616
Time/batch (s) ↓	0.043	0.085	0.103	0.039

Table 5: Efficiency comparison on the dielectric dataset.

	MEGNET	ETGNN	GMTNet	GoeCTP (Ours)
Total Time (s) ↓	943	1220	5771	938
Time/batch (s) ↓	0.060	0.078	0.370	0.060

Table 6: Efficiency comparison on the piezoelectric dataset.

	MEGNET	ETGNN	GMTNet	GoeCTP (Ours)
Total Time (s) ↓	2899	4448	> 36000	2422
Time/batch (s) ↓	0.036	0.056	> 0.452	0.030

Table 7: Efficiency comparison on the elastic dataset.

serves as a plug-and-play module that can be integrated with any existing scalar property prediction network, enabling it to predict tensor properties with negligible additional computational cost. The proposed approach achieves state-of-the-art predictive performance and superior efficiency across a variety of widely used benchmark datasets for crystal tensor properties.

Except for the excel performance, our current *GoeCTP* has some limitations remain, which include (1) The performance of *GoeCTP* is inherently dependent on the performance of the Prediction module. (2) *GoeCTP* is specifically tailored for the prediction of tensor properties in crystalline materials and has not yet been adapted for other material types (See Appendix A.12 for more limitations details). In future study, we intend to improve performance by integrating prior knowledge related to the independent components of tensor properties across various crystal systems (see Appendix A.9). Further discussion on the utilization of space group constraints on tensor properties can be found in Appendix A.13.

References

- [1] C. Chen, W. Ye, Y. Zuo, C. Zheng, and S. P. Ong. Graph networks as a universal machine learning framework for molecules and crystals. *Chemistry of Materials*, 31(9):3564–3572, 2019.
- [2] K. Choudhary and B. DeCost. Atomistic line graph neural network for improved materials property predictions. *npj Computational Materials*, 7(1):185, 2021.
- [3] K. Das, B. Samanta, P. Goyal, S.-C. Lee, S. Bhattacharjee, and N. Ganguly. Crysgnn: Distilling pre-trained knowledge to enhance property prediction for crystalline materials. In *Proceedings of the AAAI Conference on Artificial Intelligence*, volume 37, pages 7323–7331, 2023.
- [4] M. De Jong, W. Chen, H. Geerlings, M. Asta, and K. A. Persson. A database to enable discovery and design of piezoelectric materials. *Scientific data*, 2(1):1–13, 2015.
- [5] A. A. Duval, V. Schmidt, A. Hernández-García, S. Miret, F. D. Malliaros, Y. Bengio, and D. Rolnick. Faenet: Frame averaging equivariant gnn for materials modeling. In *International Conference on Machine Learning*, pages 9013–9033. PMLR, 2023.
- [6] N. Dym, H. Lawrence, and J. W. Siegel. Equivariant frames and the impossibility of continuous canonicalization. In *Forty-first International Conference on Machine Learning*, 2024.
- [7] M. Geiger and T. Smidt. e3nn: Euclidean neural networks. *arXiv preprint arXiv:2207.09453*, 2022.
- [8] S. Gorfman and N. Zhang. Piezoelectric coefficients and crystallographic symmetry. *Piezoelectric Materials: From Fundamentals to Emerging Applications*, 1:1–15, 2024.
- [9] B. C. Hall and B. C. Hall. *Lie groups, Lie algebras, and representations*. Springer, 2013.
- [10] R. M. Heiberger. Algorithm as 127: Generation of random orthogonal matrices. *Applied Statistics*, pages 199–206, 1978.
- [11] A. Heilman, C. Schlesinger, and Q. Yan. Equivariant graph neural networks for prediction of tensor material properties of crystals. *arXiv preprint arXiv:2406.03563*, 2024.
- [12] N. J. Higham. Computing the polar decomposition—with applications. *SIAM Journal on Scientific and Statistical Computing*, 7(4):1160–1174, 1986.
- [13] E. Hoogetboom, V. G. Satorras, C. Vignac, and M. Welling. Equivariant diffusion for molecule generation in 3d. In *International conference on machine learning*, pages 8867–8887. PMLR, 2022.
- [14] Y. Itin and F. W. Hehl. The constitutive tensor of linear elasticity: its decompositions, cauchy relations, null lagrangians, and wave propagation. *Journal of Mathematical Physics*, 54(4), 2013.
- [15] Y. Ito, T. Taniai, R. Igarashi, Y. Ushiku, and K. Ono. Rethinking the role of frames for se(3)-invariant crystal structure modeling. In *The Thirteenth International Conference on Learning Representations*, 2025.
- [16] R. Jiao, W. Huang, Y. Liu, D. Zhao, and Y. Liu. Space group constrained crystal generation. In *The Twelfth International Conference on Learning Representations*, 2024.
- [17] S.-O. Kaba, A. K. Mondal, Y. Zhang, Y. Bengio, and S. Ravanbakhsh. Equivariance with learned canonicalization functions. In *International Conference on Machine Learning*, pages 15546–15566. PMLR, 2023.
- [18] W. Kabsch. A solution for the best rotation to relate two sets of vectors. *Acta Crystallographica Section A: Crystal Physics, Diffraction, Theoretical and General Crystallography*, 32(5):922–923, 1976.
- [19] J. Lawrence, J. Bernal, and C. Witzgall. A purely algebraic justification of the kabsch-umeyama algorithm. *Journal of research of the National Institute of Standards and Technology*, 124:1, 2019.
- [20] N. Lee, H. Noh, S. Kim, D. Hyun, G. S. Na, and C. Park. Density of states prediction of crystalline materials via prompt-guided multi-modal transformer. *Advances in Neural Information Processing Systems*, 36, 2024.
- [21] Y. Lin, K. Yan, Y. Luo, Y. Liu, X. Qian, and S. Ji. Efficient approximations of complete interatomic potentials for crystal property prediction. In *International Conference on Machine Learning*, pages 21260–21287. PMLR, 2023.
- [22] Y. Lin, J. Helwig, S. Gui, and S. Ji. Equivariance via minimal frame averaging for more symmetries and efficiency. In *Forty-first International Conference on Machine Learning*, 2024.

- [23] P. Lippmann, G. Gerhartz, R. Remme, and F. A. Hamprecht. Beyond canonicalization: How tensorial messages improve equivariant message passing. In *The Thirteenth International Conference on Learning Representations*, 2025.
- [24] I. Loshchilov and F. Hutter. Decoupled weight decay regularization. In *International Conference on Learning Representations*, 2018.
- [25] Y. Lou and A. M. Ganose. Discovery of highly anisotropic dielectric crystals with equivariant graph neural networks. *arXiv preprint arXiv:2405.07915*, 2024.
- [26] S.-Y. Louis, Y. Zhao, A. Nasiri, X. Wang, Y. Song, F. Liu, and J. Hu. Graph convolutional neural networks with global attention for improved materials property prediction. *Physical Chemistry Chemical Physics*, 22(32):18141–18148, 2020.
- [27] G. Ma, Y. Wang, D. Lim, S. Jegelka, and Y. Wang. A canonicalization perspective on invariant and equivariant learning. In *The Thirty-eighth Annual Conference on Neural Information Processing Systems*, 2024.
- [28] Z. Mao, W. Li, and J. Tan. Dielectric tensor prediction for inorganic materials using latent information from preferred potential. *npj Computational Materials*, 10(1):265, 2024.
- [29] K. Martinkus, J. Ludwiczak, W.-C. Liang, J. Lafrance-Vanasse, I. Hotzel, A. Rajpal, Y. Wu, K. Cho, R. Bonneau, V. Gligorijevic, et al. Abdiffuser: full-atom generation of in-vitro functioning antibodies. *Advances in Neural Information Processing Systems*, 36:40729–40759, 2023.
- [30] K. Momma and F. Izumi. Vesta 3 for three-dimensional visualization of crystal, volumetric and morphology data. *Journal of applied crystallography*, 44(6):1272–1276, 2011.
- [31] K. Morita, D. W. Davies, K. T. Butler, and A. Walsh. Modeling the dielectric constants of crystals using machine learning. *The Journal of Chemical Physics*, 153(2), 2020.
- [32] K. S. Novoselov, D. Jiang, F. Schedin, T. Booth, V. Khotkevich, S. Morozov, and A. K. Geim. Two-dimensional atomic crystals. *Proceedings of the National Academy of Sciences*, 102(30):10451–10453, 2005.
- [33] J. F. Nye. *Physical properties of crystals: their representation by tensors and matrices*. Oxford university press, 1985.
- [34] T. Pakornchote, A. Ektarawong, and T. Chotibut. Straintensornet: Predicting crystal structure elastic properties using se (3)-equivariant graph neural networks. *Physical Review Research*, 5(4):043198, 2023.
- [35] I. Petousis, W. Chen, G. Hautier, T. Graf, T. D. Schladt, K. A. Persson, and F. B. Prinz. Benchmarking density functional perturbation theory to enable high-throughput screening of materials for dielectric constant and refractive index. *Physical Review B*, 93(11):115151, 2016.
- [36] O. Puny, M. Atzmon, E. J. Smith, I. Misra, A. Grover, H. Ben-Hamu, and Y. Lipman. Frame averaging for invariant and equivariant network design. In *International Conference on Learning Representations*, 2022.
- [37] Z. Ran, C. Zou, Z. Wei, and H. Wang. Velas: An open-source toolbox for visualization and analysis of elastic anisotropy. *Computer Physics Communications*, 283:108540, 2023.
- [38] R. Resta. Macroscopic polarization in crystalline dielectrics: the geometric phase approach. *Reviews of modern physics*, 66(3):899, 1994.
- [39] P. C. Sherrell, M. Fronzi, N. A. Shepelin, A. Corletto, D. A. Winkler, M. Ford, J. G. Shapter, and A. V. Ellis. A bright future for engineering piezoelectric 2d crystals. *Chemical Society Reviews*, 51(2):650–671, 2022.
- [40] Y. Song, J. Gong, M. Xu, Z. Cao, Y. Lan, S. Ermon, H. Zhou, and W.-Y. Ma. Equivariant flow matching with hybrid probability transport for 3d molecule generation. *Advances in Neural Information Processing Systems*, 36, 2024.
- [41] G. K. Tam, Z.-Q. Cheng, Y.-K. Lai, F. C. Langbein, Y. Liu, D. Marshall, R. R. Martin, X.-F. Sun, and P. L. Rosin. Registration of 3d point clouds and meshes: A survey from rigid to nonrigid. *IEEE transactions on visualization and computer graphics*, 19(7):1199–1217, 2012.
- [42] T. Taniai, R. Igarashi, Y. Suzuki, N. Chiba, K. Saito, Y. Ushiku, and K. Ono. Crystalformer: Infinitely connected attention for periodic structure encoding. In *The Twelfth International Conference on Learning Representations*, 2024.

- [43] X. Wang and M. Zhang. Graph neural network with local frame for molecular potential energy surface. In *Learning on Graphs Conference*, pages 19–1. PMLR, 2022.
- [44] Y. Wang, S. Kong, J. M. Gregoire, and C. P. Gomes. Conformal crystal graph transformer with robust encoding of periodic invariance. In *Proceedings of the AAAI Conference on Artificial Intelligence*, volume 38, pages 283–291, 2024.
- [45] Z. Wang, H. Hua, W. Lin, M. Yang, and K. C. Tan. Crystalline material discovery in the era of artificial intelligence. *arXiv preprint arXiv:2408.08044*, 2024.
- [46] M. Wen, M. K. Horton, J. M. Munro, P. Huck, and K. A. Persson. An equivariant graph neural network for the elasticity tensors of all seven crystal systems. *Digital Discovery*, 3(5):869–882, 2024.
- [47] T. Xie and J. C. Grossman. Crystal graph convolutional neural networks for an accurate and interpretable prediction of material properties. *Physical review letters*, 120(14):145301, 2018.
- [48] M. Xu, J. Han, A. Lou, J. Kossaifi, A. Ramanathan, K. Azizzadenesheli, J. Leskovec, S. Ermon, and A. Anandkumar. Equivariant graph neural operator for modeling 3d dynamics. In *Forty-first International Conference on Machine Learning*, 2024.
- [49] K. Yan, Y. Liu, Y. Lin, and S. Ji. Periodic graph transformers for crystal material property prediction. *Advances in Neural Information Processing Systems*, 35:15066–15080, 2022.
- [50] K. Yan, C. Fu, X. Qian, X. Qian, and S. Ji. Complete and efficient graph transformers for crystal material property prediction. In *The Twelfth International Conference on Learning Representations*, 2024.
- [51] K. Yan, A. Saxton, X. Qian, X. Qian, and S. Ji. A space group symmetry informed network for $o(3)$ equivariant crystal tensor prediction. In *Forty-first International Conference on Machine Learning*, 2024.
- [52] Z. Zheng, Y. Liu, J. Li, J. Yao, and Y. Rong. Relaxing continuous constraints of equivariant graph neural networks for broad physical dynamics learning. In *Proceedings of the 30th ACM SIGKDD Conference on Knowledge Discovery and Data Mining*, pages 4548–4558, 2024.
- [53] Y. Zhong, H. Yu, X. Gong, and H. Xiang. A general tensor prediction framework based on graph neural networks. *The Journal of Physical Chemistry Letters*, 14(28):6339–6348, 2023.

A Appendix

A.1 Related work

GNN-Based Methods. CGCNN is a pioneering GNN model specifically designed for handling crystal structures [47]. This model proposed to represent crystal structures as multi-edge crystal graphs. It was applied to predict various single-value properties such as formation energy and band gap. Since then, several GNN methods have been developed to improve upon CGCNN through exploring various network designs or leveraging prior knowledge [1, 26, 2, 3, 21]. These GNN methods are primarily designed for single-value property prediction and do not address the prediction of high-order tensor properties, such as dielectric or elastic tensors. Furthermore, they lack the ability to preserve the equivariance required for accurate high-order tensor property prediction. In contrast, recent studies attempted to ensure equivariance through specialized network architectures [28, 25, 11, 46, 34, 51, 53]. These approaches generally employ harmonic decomposition to achieve equivariance for tensor properties. Within these network architectures, many operations are required, such as tensor products and combining irreducible representations. These processes significantly increase computational costs, especially when handling higher-order data.

Transformer-Based Methods. Transformers, with their self-attention mechanism and parallel processing capabilities, are particularly well-suited for predicting crystal material properties. MatFormer [49], one of the earliest Transformer-based networks used for crystal material property prediction, encoded crystal periodic patterns by using the geometric distances between the same atoms in neighboring unit cells. This addressed the issue in earlier GNN-based methods, including CGCNN, MEGNet, GATGNN, and others, which neglected the periodic patterns of infinite crystal structures. Subsequently, more advanced Transformer-based approaches were proposed. Some methods, such as ComFormer [50], CrystalFormer [44], and CrystalFormer [42], typically incorporate either enhanced graph construction techniques or physical priors, exhibiting impressive results in the prediction of single-value properties. Furthermore, DOSTransformer [20] is tailored for the density of states prediction, utilizing prompt-guided multi-modal transformer architecture to achieve super performance. Nevertheless, these models are not directly applicable for accurate high-order tensor property prediction due to their inability to capture the necessary equivariance.

Equivariant Learning. Recently, two general-purpose equivariant learning techniques for the arbitrary group have gained widespread attention: frame averaging [22, 36, 5] and canonicalization [27, 17, 6]. Frame averaging is developed based on group averaging and involves averaging over smaller frames instead of the entire group. Canonicalization, on the other hand, is inherently related to frame averaging and can be viewed as a more general form of it. [27]. In particular, Lin et al. [22] introduced minimal frame averaging, a method designed to achieve both efficient and exact equivalence in equivariant learning. This approach is primarily applicable to scenarios where the input and output spaces are identical, such as the n-body problem. It does not extend to cases involving different spaces, such as crystal tensor prediction. If this method were extended to tensor property prediction, it would represent a special case of Proposition 3.4, where both orbit canonicalization and rigid registration are achieved using QR decomposition. Within Proposition 3.4, however, different functions can be employed for orbit canonicalization and rigid registration. For instance, the Kabsch algorithm [18, 19] can be employed for rigid registration, while polar decomposition can be utilized for canonicalization.

To the best of our knowledge, no previous work has extended these equivariant learning techniques to the prediction of crystal tensor properties. Thus, our method represents the first extension of these concepts to the crystal tensor property prediction.

A.2 Details of Framework Architecture

Crystal Graph Construction. In *GoeCTP*, we use the crystal graph construction from Yan et al. [50, 51] to describe the structure and relationships within crystals. Specifically, we first convert the fractional coordinate system $(\mathbf{A}, \mathbf{F}, \mathbf{H})$ into the Cartesian coordinate system $(\mathbf{A}, \mathbf{X}, \mathbf{H})$ as introduced in Section 2. Then, we assume that the output crystal graph is represented as $\mathcal{G}(\mathcal{V}, \mathcal{E})$, \mathcal{V} denotes the set of nodes v_i in the crystal graph, where each node v_i contains atomic features $\mathbf{v}_i = (\mathbf{a}_i, \hat{\mathbf{p}}_i)$. \mathcal{E} represents the set of edges denoted as e_{ij} , which are typically constructed based on the Euclidean distance d_{ij} between nodes v_i and v_j . When the Euclidean distance d_{ij} between nodes v_i and v_j is less than a given radius R , i.e. $d_{ij} = \|\mathbf{p}_j + k_1\mathbf{l}_1 + k_2\mathbf{l}_2 + k_3\mathbf{l}_3 - \mathbf{p}_i\|_2 \leq R$, an edge e_{ij} will be built

with edge feature $\mathbf{e}_{ij} = \mathbf{p}_j + k_1 \mathbf{l}_1 + k_2 \mathbf{l}_2 + k_3 \mathbf{l}_3 - \mathbf{p}_i$. Here, R is established based on the distance to the k -th nearest neighbor, and different values of $\mathbf{k} = [k_1, k_2, k_3] \in \mathbb{Z}^3$ represent different edges between nodes v_i and v_j . Since there are no equivariance requirements for subsequent models, any other graph construction methods can be used to replace this part, such as Wang et al. [44], Yan et al. [50].

eComFormer. The eComFormer has demonstrated strong performance across a range of single-value property prediction tasks [50]. It is built on an SO(3)-equivariant crystal graph representation, where the interatomic distance vectors are employed to represent the edge features of the graph. The model converts this crystal graph into embeddings and utilizes a transformer architecture, incorporating both a node-wise transformer layer and a node-wise equivariant updating layer, to extract rich geometric information during the message-passing process.

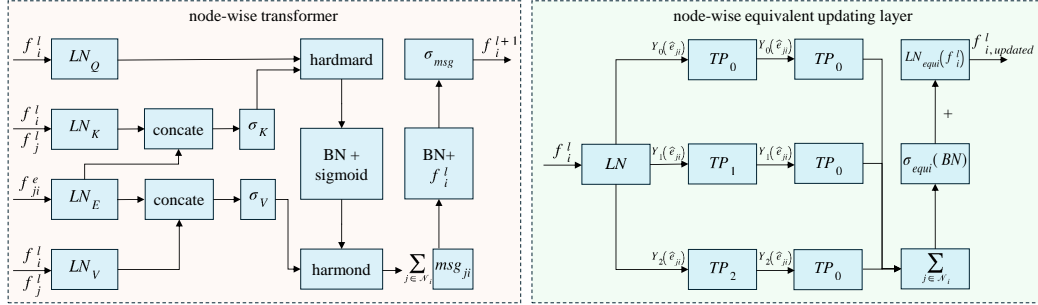


Figure 3: The detailed architectures of the node-wise transformer layer and node-wise equivariant updating layer, adapted from Yan et al. [50].

Specifically, the node-wise transformer layer is responsible for updating the node-invariant features \mathbf{f}_i . This process utilizes the node features \mathbf{f}_i , neighboring node features \mathbf{f}_j , and edge features \mathbf{f}_{ij} to facilitate message passing from neighboring node j to the central node i , followed by aggregation of all neighboring messages to update \mathbf{f}_i . The update mechanism is structured similarly to a transformer. Firstly, the message from node j to node i is transformed into corresponding query $\mathbf{q}_{ij} = \text{LN}_Q(\mathbf{f}_i)$, key $\mathbf{k}_{ij} = (\text{LN}_K(\mathbf{f}_i) | \text{LN}_K(\mathbf{f}_j))$, and value feature $\mathbf{v}_{ij} = (\text{LN}_V(\mathbf{f}_i) | \text{LN}_V(\mathbf{f}_j) | \text{LN}_E(\mathbf{f}_{ij}^e))$, where $\text{LN}_Q(\cdot)$, $\text{LN}_K(\cdot)$, $\text{LN}_V(\cdot)$, $\text{LN}_E(\cdot)$ denote the linear transformations, and $|$ denote the concatenation. Then, the self-attention output is then computed as:

$$\alpha_{ij} = \frac{\mathbf{q}_{ij} \circ \xi_K(\mathbf{k}_{ij})}{\sqrt{d_{\mathbf{q}_{ij}}}}, \mathbf{msg}_{ij} = \text{sigmoid}(\text{BN}(\alpha_{ij})) \circ \xi_V(\mathbf{v}_{ij}), \quad (8)$$

where ξ_K , ξ_V represent nonlinear transformations applied to key and value features, respectively. The operators \circ denote the Hadamard product, $\text{BN}(\cdot)$ refers to the batch normalization layer, and $\sqrt{d_{\mathbf{q}_{ij}}}$ indicates the dimensionality of \mathbf{q}_{ij} . Then, node feature \mathbf{f}_i is updated as follows,

$$\mathbf{msg}_i = \sum_{j \in \mathcal{N}_i} \mathbf{msg}_{ij}, \mathbf{f}_i^{\text{new}} = \xi_{\text{msg}}(\mathbf{f}_i + \text{BN}(\mathbf{msg}_i)), \quad (9)$$

where $\xi_{\text{msg}}(\cdot)$ denoting the softplus activation function.

The node-wise equivariant updating layer is designed to effectively capture geometric features by incorporating node feature \mathbf{a}_i and edge feature $\|\mathbf{e}_{ji}\|_2$ as inputs and stacking two tensor product (TP) layers [7]. It uses node feature \mathbf{f}_i^l and equivalent vector feature \mathbf{e}_{ji} embedded by corresponding spherical harmonics $\mathbf{Y}_0(\hat{\mathbf{e}}_{ji}) = c_0$, $\mathbf{Y}_1(\hat{\mathbf{e}}_{ji}) = c_1 \frac{\mathbf{e}_{ji}}{\|\mathbf{e}_{ji}\|_2} \in \mathbb{R}^3$ and $\mathbf{Y}_2(\hat{\mathbf{e}}_{ji}) \in \mathbb{R}^5$ to represent the input features. Gathering rotational information from neighboring nodes to the central node i , the first TP layer is shown as

$$\mathbf{f}_{i,0}^l = \mathbf{f}_i^{l'} + \frac{1}{|\mathcal{N}_i|} \sum_{j \in \mathcal{N}_i} \text{TP}_0(\mathbf{f}_j^{l'}, \mathbf{Y}_0(\hat{\mathbf{e}}_{ji})), \mathbf{f}_{i,\lambda}^l = \frac{1}{|\mathcal{N}_i|} \sum_{j \in \mathcal{N}_i} \text{TP}_\lambda(\mathbf{f}_j^{l'}, \mathbf{Y}_\lambda(\hat{\mathbf{e}}_{ji})), \lambda \in \{1, 2\}, \quad (10)$$

where $\mathbf{f}_i^{l'}$ is linearly transformed from \mathbf{f}_i^l , $|\mathcal{N}_i|$ and \mathbf{TP}_λ represent the number of neighbors of node i and TP layers with rotation order λ respectively. Then, to represent the invariant node features, the second TP layer is written as

$$\mathbf{f}_i^{l*} = \frac{1}{|\mathcal{N}_i|} \left(\sum_{j \in \mathcal{N}_i} \mathbf{TP}_0(\mathbf{f}_{j,0}^l, \mathbf{Y}_0(\hat{\mathbf{e}}_{ji})) + \sum_{j \in \mathcal{N}_i} \mathbf{TP}_0(\mathbf{f}_{j,1}^l, \mathbf{Y}_1(\hat{\mathbf{e}}_{ji})) + \sum_{j \in \mathcal{N}_i} \mathbf{TP}_0(\mathbf{f}_{j,2}^l, \mathbf{Y}_2(\hat{\mathbf{e}}_{ji})) \right), \quad (11)$$

stacking the two tensor product layers together using both linear and nonlinear transformations, the output $\mathbf{f}_{i,updated}^l$ is combined as

$$\mathbf{f}_{i,updated}^l = \sigma_{\text{equi}}(\text{BN}(\mathbf{f}_i^{l*})) + \text{LN}_{\text{equi}}(\mathbf{f}_i^l), \quad (12)$$

with σ_{equi} denoting a nonlinear transformation made up of two softplus layers with a linear layer positioned between them. The detailed architectures of the node-wise transformer layer and node-wise equivariant updating layer are shown in Fig. 3.

A.3 Proofs

A.4 Proofs of Lemma A.1

Lemma A.1. *Given a orbit canonicalization function $C_{\mathbf{M}}(\cdot)$, for any prediction function $f_\theta(\cdot)$, it holds that $f_\theta(C_{\mathbf{M}}(\cdot))$ is $O(3)$ -invariant.*

Proof. According to Definition 3.2, for any $g \in O(3)$ and $\mathbf{M} \in \mathcal{V}$, we have $C_{\mathbf{M}}(\mathbf{M}) = \mathbf{M}_0$ and $C_{\mathbf{M}}(g \cdot \mathbf{M}) = \mathbf{M}_0$. Thus,

$$\begin{aligned} f_\theta(C_{\mathbf{M}}(g \cdot \mathbf{M})) &= f_\theta(\mathbf{M}_0) \\ &= f_\theta(C_{\mathbf{M}}(\mathbf{M})), \end{aligned} \quad (13)$$

which implies $f_\theta(C_{\mathbf{M}}(\cdot))$ is $O(3)$ -invariant. \square

A.5 Proofs of Lemma A.2

Lemma A.2. *For a rigid registration function $R_{\mathbf{M}}(\mathbf{M}_1, \mathbf{M}_2) = g$, it is $O(3)$ -equivariant with respect to the input \mathbf{M}_1 .*

Proof. According to Definition 3.3, $\mathbf{M}_1 = R_{\mathbf{M}}(\mathbf{M}_1, \mathbf{M}_2) \cdot \mathbf{M}_2$. Thus, for any $g \in O(3)$, we have

$$\begin{aligned} R_{\mathbf{M}}(g \cdot \mathbf{M}_1, \mathbf{M}_2) \cdot \mathbf{M}_2 &= g \cdot \mathbf{M}_1 \\ &= g \cdot (R_{\mathbf{M}}(\mathbf{M}_1, \mathbf{M}_2) \cdot \mathbf{M}_2) \\ &= (g \cdot R_{\mathbf{M}}(\mathbf{M}_1, \mathbf{M}_2)) \cdot \mathbf{M}_2. \end{aligned} \quad (14)$$

Given $\mathbf{M}_2 = (\mathbf{A}_2, \mathbf{F}_2, \mathbf{L}_2)$, and noting that $g \cdot \mathbf{M}_2 = (\mathbf{A}_2, \mathbf{F}_2, \mathbf{Q}\mathbf{L}_2)$ (where \mathbf{L}_2 has full rank), we can write Eq. 14 as

$$(R_{\mathbf{M}}(g \cdot \mathbf{M}_1, \mathbf{M}_2))\mathbf{L}_2 = (g \cdot R_{\mathbf{M}}(\mathbf{M}_1, \mathbf{M}_2))\mathbf{L}_2. \quad (15)$$

Therefore, $R_{\mathbf{M}}(g \cdot \mathbf{M}_1, \mathbf{M}_2) = g \cdot R_{\mathbf{M}}(\mathbf{M}_1, \mathbf{M}_2)$, which implies that $R_{\mathbf{M}}(\mathbf{M}_1, \mathbf{M}_2)$ is $O(3)$ -equivariant. \square

A.6 Proof of Proposition 3.4

Proposition 3.4. *($O(3)$ -Equivariant Tensor Prediction from the Perspective of Canonicalization.) Given an arbitrary tensor prediction function $f(\mathbf{M}) : \mathcal{V} \rightarrow \mathcal{W}$, we can define a new function $h(\mathbf{M}) = R_{\mathbf{M}}(\mathbf{M}, C_{\mathbf{M}}(\mathbf{M})) \cdot f(C_{\mathbf{M}}(\mathbf{M}))$, such that $h(\mathbf{M})$ is $O(3)$ equivariant for tensor prediction.*

Proof. According to Lemma A.2 and Lemma A.1, for any $g \in O(3)$ we have

$$\begin{aligned} h(g \cdot \mathbf{M}) &= R_{\mathbf{M}}(g \cdot \mathbf{M}, C_{\mathbf{M}}(g \cdot \mathbf{M})) \cdot f(C_{\mathbf{M}}(g \cdot \mathbf{M})) \\ &= R_{\mathbf{M}}(g \cdot \mathbf{M}, C_{\mathbf{M}}(\mathbf{M})) \cdot f(C_{\mathbf{M}}(\mathbf{M})) \\ &= g \cdot R_{\mathbf{M}}(\mathbf{M}, C_{\mathbf{M}}(\mathbf{M})) \cdot f(C_{\mathbf{M}}(\mathbf{M})) \\ &= g \cdot h(\mathbf{M}) \end{aligned} \quad (16)$$

\square

Thus, $h(\mathbf{M})$ is $O(3)$ equivariant for tensor prediction.

A.7 Proof of Proposition 3.6

Proposition 3.6. (*Orbit Canonicalization and Rigid Registration for Crystal Tensor Prediction.*) By performing polar decomposition on the lattice matrix $\mathbf{L} = \mathbf{QH}$ of a crystal \mathbf{M} , we can define functions $f_{p1}(\mathbf{M}) = (\mathbf{A}, \mathbf{F}, \mathbf{H})$ and $f_{p2}(\mathbf{M}, f_{p1}(\mathbf{M})) = \mathbf{Q}$, where $f_{p1}(\cdot)$ and $f_{p2}(\cdot)$ correspond to performing polar decomposition on the lattice matrix. In this perspective, $f_{p1}(\cdot)$ serve as the orbit canonicalization function, while $f_{p2}(\cdot)$ serve as the rigid registration function. The matrix \mathbf{H} is thus identified as the canonical form.

Proof. Given the lattice matrices \mathbf{L} and $\mathbf{Q}'\mathbf{L}$, where \mathbf{Q}' is an arbitrary $O(3)$ group transformation, applying polar decomposition on both \mathbf{L} and $\mathbf{Q}'\mathbf{L}$ yields the following expressions:

$$\mathbf{L} = \mathbf{QH} \quad (17)$$

$$\mathbf{Q}'\mathbf{L} = \mathbf{Q}_1\mathbf{H}_1. \quad (18)$$

By combining Eq. 17 and 18, we can have the following equation:

$$\mathbf{Q}'\mathbf{QH} = \mathbf{Q}_1\mathbf{H}_1. \quad (19)$$

Because $\mathbf{Q}'\mathbf{Q}(\mathbf{Q}'\mathbf{Q})^\top = \mathbf{Q}'\mathbf{Q}\mathbf{Q}^\top\mathbf{Q}'^\top = \mathbf{I}$, it follows that $\mathbf{Q}'\mathbf{Q}$ is an orthogonal matrix. According to the uniqueness of polar decomposition, we can have $\mathbf{Q}'\mathbf{Q} = \mathbf{Q}_1$, which implies $\mathbf{Q}_1\mathbf{H} = \mathbf{Q}_1\mathbf{H}_1$. If $\mathbf{H}_1 \neq \mathbf{H}$, this would violate the uniqueness property of polar decomposition. Therefore, we conclude that $\mathbf{H}_1 = \mathbf{H}$, indicating that \mathbf{H} remains unaffected by the $O(3)$ group transformation. Consequently, the crystal configuration $\mathbf{M}_0 = (\mathbf{A}, \mathbf{F}, \mathbf{H})$ can serve as the canonical form. Performing polar decomposition on the lattice matrix to obtain $\mathbf{M}_0 = (\mathbf{A}, \mathbf{F}, \mathbf{H})$, i.e. $f_{p1}(\mathbf{M}) = (\mathbf{A}, \mathbf{F}, \mathbf{H})$, can thus be regarded as the orbit canonicalization function. Furthermore, based on Eq. 17, performing polar decomposition on the lattice matrix to obtain \mathbf{Q} , i.e. $f_{p2}(\mathbf{M}, \mathbf{M}_0) = \mathbf{Q}$, can be regarded as rigid registration function, as shown below:

$$\mathbf{L} = \mathbf{QH} \rightarrow \mathbf{M} = \mathbf{QM}_0 \rightarrow \mathbf{M} = f_{p2}(\mathbf{M}, \mathbf{M}_0) \cdot \mathbf{M}_0. \quad (20)$$

□

A.8 $O(3)$ equivariance for crystal tensor properties

Due to the difference between the input space \mathcal{V} and the output space \mathcal{W} , the $O(3)$ equivariance required for crystal tensor property prediction tasks differs from the $O(3)$ equivariance typically encountered in general molecular studies [13, 48, 40]. In molecular studies, the input space \mathcal{V} and the output space \mathcal{W} are the same, meaning group representations in these spaces are identical, i.e. $\rho_{\mathcal{V}}(g) = \rho_{\mathcal{W}}(g)$. Specifically, for a function $f(\mathbf{X})$, if it is $O(3)$ equivariant, then it satisfies $f(\mathbf{QX}) = \mathbf{Q}f(\mathbf{X})$, where $\mathbf{Q} \in \mathbb{R}^{3 \times 3}$ is an arbitrary orthogonal matrix, and $\mathbf{X} \in \mathbb{R}^{3 \times N}$ represents the coordinate matrix of atoms in a molecule. In this context, the function f can be seen as the model. However, in the prediction of crystal tensor properties, the requirements for $O(3)$ equivariance differ. In what follows, we will provide a detailed introduction to this difference.

Dielectric tensor. For the dielectric tensor $\varepsilon \in \mathbb{R}^{3 \times 3}$ and a function $f : (\mathbf{A}, \mathbf{F}, \mathbf{L}) \rightarrow \varepsilon$, if it is $O(3)$ equivariant, it must satisfy $f(\mathbf{A}, \mathbf{F}, \mathbf{QL}) = \mathbf{Q}f(\mathbf{A}, \mathbf{F}, \mathbf{L})\mathbf{Q}^\top$. The reason for this difference lies in the physical nature of the dielectric tensor, which characterizes a material's polarization response to an external electric field [51]. Specifically, the dielectric tensor describes the relationship between the electric displacement $\mathbf{D} \in \mathbb{R}^3$ and the applied electric field $\mathbf{E} \in \mathbb{R}^3$ through the equation $\mathbf{D} = \varepsilon\mathbf{E}$. When an $O(3)$ group transformation \mathbf{Q} is applied to the crystal structure, the relationship $\mathbf{D}' = \varepsilon'\mathbf{E}'$ holds, where $\mathbf{D}' = \mathbf{QD}$ and $\mathbf{E}' = \mathbf{QE}$. Substituting these into the equation, we have:

$$\mathbf{QD} = \varepsilon'\mathbf{QE} \rightarrow \mathbf{D} = \mathbf{Q}^\top\varepsilon'\mathbf{QE}, \quad (21)$$

which implies that the dielectric tensor transforms under the $O(3)$ group transformation as: $\varepsilon' = \mathbf{Q}\varepsilon\mathbf{Q}^\top$. This transformation principle extends similarly to other crystal tensors, as follows.

Piezoelectric tensor. The piezoelectric tensor $\mathbf{e} \in \mathbb{R}^{3 \times 3 \times 3}$ describes the relationship between the applied strain $\epsilon \in \mathbb{R}^{3 \times 3}$ to the electric displacement field $\mathbf{D} \in \mathbb{R}^3$ within the material. Mathematically, this relationship is expressed as $\mathbf{D}_i = \sum_{jk} \mathbf{e}_{ijk} \epsilon_{jk}$, with $i, j, k \in \{1, 2, 3\}$.

When an $O(3)$ group transformation \mathbf{Q} is applied to the crystal, the strain tensor and electric displacement field is transformed to $\epsilon'_{jk} = \sum_{mn} \mathbf{Q}_{jm} \mathbf{Q}_{kn} \epsilon_{mn}$ and $\mathbf{D}'_i = \sum_{\ell} \mathbf{Q}_{i\ell} \mathbf{D}_{\ell}$. The relation is then reformulated as $\mathbf{D}'_i = \sum_{jk} \mathbf{e}'_{ijk} \epsilon'_{jk}$. Since \mathbf{Q} is orthogonal matrix ($\mathbf{Q}^{-1} = \mathbf{Q}^{\top}$), we have $\epsilon_{jk} = \sum_{mn} \mathbf{Q}_{mj} \mathbf{Q}_{nk} \epsilon'_{mn}$. Consequently, \mathbf{D}'_i can be represented as

$$\begin{aligned}
\mathbf{D}'_i &= \sum_{\ell} \mathbf{Q}_{i\ell} \mathbf{D}_{\ell} \\
&= \sum_{\ell} \mathbf{Q}_{i\ell} \sum_{jk} \mathbf{e}_{\ell jk} \epsilon_{jk} \\
&= \sum_{\ell} \mathbf{Q}_{i\ell} \sum_{jk} \mathbf{e}_{\ell jk} \left(\sum_{mn} \mathbf{Q}_{mj} \mathbf{Q}_{nk} \epsilon'_{mn} \right) \\
&= \sum_{\ell} \mathbf{Q}_{i\ell} \sum_{mn} \mathbf{e}_{\ell mn} \left(\sum_{jk} \mathbf{Q}_{jm} \mathbf{Q}_{kn} \epsilon'_{jk} \right) \quad (\text{exchange sign, } m \leftrightarrow j, n \leftrightarrow k) \\
&= \sum_{jk} \sum_{lmn} \mathbf{Q}_{il} \mathbf{Q}_{jm} \mathbf{Q}_{kn} \mathbf{e}_{lmn} \epsilon'_{jk}
\end{aligned} \tag{22}$$

Therefore, under the $O(3)$ group transformation \mathbf{Q} , the transformed piezoelectric tensor \mathbf{e}'_{ijk} is given by:

$$\mathbf{e}'_{ijk} = \sum_{lmn} \mathbf{Q}_{il} \mathbf{Q}_{jm} \mathbf{Q}_{kn} \mathbf{e}_{lmn}. \tag{23}$$

When employing GoeCTP to predict the piezoelectric tensor, Equation 7 becomes $\mathbf{e}_{ijk}^{\text{final}} = \sum_{lmn} \mathbf{Q}_{il} \mathbf{Q}_{jm} \mathbf{Q}_{kn} \mathbf{e}_{lmn}$.

Elastic tensor. The elastic tensor $C \in \mathbb{R}^{3 \times 3 \times 3 \times 3}$ describes the relationship between the applied strain $\epsilon \in \mathbb{R}^{3 \times 3}$ and the stress tensor $\sigma \in \mathbb{R}^{3 \times 3}$ within the material. This relationship is expressed as $\sigma_{ij} = \sum_{kl} C_{ijkl} \epsilon_{kl}$, with $i, j, k, \ell \in \{1, 2, 3, 4\}$.

When an $O(3)$ group transformation \mathbf{Q} is applied to the crystal, the strain tensor and stress tensor is transformed to $\epsilon'_{jk} = \sum_{mn} \mathbf{Q}_{jm} \mathbf{Q}_{kn} \epsilon_{mn}$ and $\sigma'_{jk} = \sum_{mn} \mathbf{Q}_{jm} \mathbf{Q}_{kn} \sigma_{mn}$. Under this transformation, the relationship becomes $\sigma'_{ij} = \sum_{kl} C'_{ijkl} \epsilon'_{kl}$. Since \mathbf{Q} is orthogonal matrix ($\mathbf{Q}^{-1} = \mathbf{Q}^{\top}$), we have $\epsilon_{jk} = \sum_{mn} \mathbf{Q}_{mj} \mathbf{Q}_{nk} \epsilon'_{mn}$. Based on above equations, the transformed stress tensor σ'_{ij} can be expressed as:

$$\begin{aligned}
\sigma'_{ij} &= \sum_{mn} \mathbf{Q}_{im} \mathbf{Q}_{jn} \sigma_{mn} \\
&= \sum_{mn} \mathbf{Q}_{im} \mathbf{Q}_{jn} \sum_{pq} C_{mnpq} \epsilon_{pq} \\
&= \sum_{mn} \mathbf{Q}_{im} \mathbf{Q}_{jn} \sum_{pq} C_{mnpq} \sum_{kl} \mathbf{Q}_{kp} \mathbf{Q}_{lq} \epsilon'_{kl} \\
&= \sum_{kl} \sum_{mnpq} \mathbf{Q}_{im} \mathbf{Q}_{jn} \mathbf{Q}_{kp} \mathbf{Q}_{lq} C_{mnpq} \epsilon'_{kl}
\end{aligned} \tag{24}$$

Therefore, under the $O(3)$ group transformation \mathbf{Q} , C'_{ijkl} is represented as:

$$C'_{ijkl} = \sum_{mnpq} \mathbf{Q}_{im} \mathbf{Q}_{jn} \mathbf{Q}_{kp} \mathbf{Q}_{lq} C_{mnpq}. \tag{25}$$

When GoeCTP is used to predict elastic tensor, Equation 7 becomes $C_{ijkl}^{\text{final}} = \sum_{mnpq} \mathbf{Q}_{im} \mathbf{Q}_{jn} \mathbf{Q}_{kp} \mathbf{Q}_{lq} C_{mnpq}$.

A.9 Tensor properties symmetry

Tensor properties describe the material's response to external physical fields (such as electric fields or mechanical stress). In materials with symmetry, this response must adhere to the symmetry

requirements of the material. As demonstrated by Yan et al. [51], when the space group transformation \mathbf{R} is applied to the corresponding crystal structure $\mathbf{M} = (\mathbf{A}, \mathbf{F}, \mathbf{L})$, the crystal remains unchanged, i.e., $(\mathbf{A}, \mathbf{F}, \mathbf{L}) = (\mathbf{A}, \mathbf{F}, \mathbf{RL})$. Therefore, the corresponding tensor properties also remain unchanged, i.e., $\epsilon = \mathbf{R}\epsilon\mathbf{R}^\top$. Thus, crystal symmetry imposes strict constraints on the components of the tensor, leading to the simplification or elimination of many components, reducing the number of independent components.

Crystal system	Number of independent elements	Dielectric tensor
Cubic	1	$\epsilon = \begin{pmatrix} \epsilon_{11} & 0 & 0 \\ 0 & \epsilon_{11} & 0 \\ 0 & 0 & \epsilon_{11} \end{pmatrix}$
Tetragonal & Hexagonal & Trigonal	2	$\epsilon = \begin{pmatrix} \epsilon_{11} & 0 & 0 \\ 0 & \epsilon_{11} & 0 \\ 0 & 0 & \epsilon_{33} \end{pmatrix}$
Orthorhombic	3	$\epsilon = \begin{pmatrix} \epsilon_{11} & 0 & 0 \\ 0 & \epsilon_{22} & 0 \\ 0 & 0 & \epsilon_{33} \end{pmatrix}$
Monoclinic	4	$\epsilon = \begin{pmatrix} \epsilon_{11} & 0 & \epsilon_{13} \\ 0 & \epsilon_{22} & 0 \\ \epsilon_{13} & 0 & \epsilon_{33} \end{pmatrix}$
Triclinic	6	$\epsilon = \begin{pmatrix} \epsilon_{11} & \epsilon_{12} & \epsilon_{13} \\ \epsilon_{12} & \epsilon_{22} & \epsilon_{23} \\ \epsilon_{13} & \epsilon_{23} & \epsilon_{33} \end{pmatrix}$

Table 8: Number of independent components in the dielectric tensor for different crystal systems.

Independent components in the dielectric tensor. The 3×3 dielectric tensor has a minimum of 1 and a maximum of 6 independent elements for various types of systems due to the crystal symmetry. The number of independent components in the dielectric tensor for different crystal systems is shown in Tabel 8 [28].

Voigt notation for elastic tensor. Similar to the dielectric tensor, the elastic tensor also has independent elements for various types of systems due to the crystal symmetry. The elastic tensor has a minimum of 3 and a maximum of 21 independent elements for various types of systems. Voigt notation is a compact way to represent these independent components of tensor properties [14]. According to the rules $11 \rightarrow 1$; $22 \rightarrow 2$; $33 \rightarrow 3$; $23, 32 \rightarrow 4$; $31, 13 \rightarrow 5$; $12, 21 \rightarrow 6$, the elastic tensor in Voigt notation is a 6×6 symmetric matrix [46, 37]:

$$C = \begin{pmatrix} C_{1111} & C_{1122} & C_{1133} & C_{1123} & C_{1131} & C_{1112} \\ C_{1122} & C_{2222} & C_{2233} & C_{2223} & C_{2231} & C_{2212} \\ C_{1133} & C_{2233} & C_{3333} & C_{3323} & C_{3331} & C_{3312} \\ C_{1123} & C_{2223} & C_{3323} & C_{2323} & C_{2331} & C_{2312} \\ C_{1131} & C_{2231} & C_{3331} & C_{2331} & C_{3131} & C_{3112} \\ C_{1112} & C_{2212} & C_{3312} & C_{2312} & C_{3112} & C_{1212} \end{pmatrix} \rightarrow \begin{pmatrix} C_{11} & C_{12} & C_{13} & C_{14} & C_{15} & C_{16} \\ C_{12} & C_{22} & C_{23} & C_{24} & C_{25} & C_{26} \\ C_{13} & C_{23} & C_{33} & C_{34} & C_{35} & C_{36} \\ C_{14} & C_{24} & C_{34} & C_{44} & C_{45} & C_{46} \\ C_{15} & C_{25} & C_{35} & C_{45} & C_{55} & C_{56} \\ C_{16} & C_{26} & C_{36} & C_{46} & C_{56} & C_{66} \end{pmatrix} \quad (26)$$

The number of independent components in the elastic tensor for different crystal systems is shown in Tabel 9 (partial data shown; for more details, refer to Wen et al. [46], Ran et al. [37]).

Voigt notation for piezoelectric tensor. The number of independent components in the piezoelectric tensor for different crystal systems is shown in Tabel 10 (partial data shown; for more details, refer to De Jong et al. [4], Gorfman and Zhang [8]).

A.10 Experimental details

Datasets details. The dataset for dielectric tensor and piezoelectric tensor is derived from the data processed by Yan et al. [51], sourced from the JARVIS-DFT database. Similarly, the dataset for elastic tensor is obtained from the *dft_3d* data within the JARVIS-DFT database². The statistical details of the datasets are presented in Table 11. Additionally, in the dielectric tensor dataset, the dielectric tensor is a 3×3 symmetric matrix. Therefore, during prediction, we predict 6 elements of the matrix (see Appendix A.9 for details) and then reconstruct the entire 3×3 symmetric matrix. In

²<https://pages.nist.gov/jarvis/databases/>

Crystal system	Number of independent elements	Elastic tensor
Cubic	3	$C = \begin{pmatrix} C_{11} & C_{12} & C_{12} & 0 & 0 & 0 \\ C_{12} & C_{11} & C_{12} & 0 & 0 & 0 \\ C_{12} & C_{12} & C_{11} & 0 & 0 & 0 \\ 0 & 0 & 0 & C_{44} & 0 & 0 \\ 0 & 0 & 0 & 0 & C_{44} & 0 \\ 0 & 0 & 0 & 0 & 0 & C_{44} \end{pmatrix}$
Tetragonal	6	$C = \begin{pmatrix} C_{11} & C_{12} & C_{13} & 0 & 0 & 0 \\ C_{12} & C_{11} & C_{13} & 0 & 0 & 0 \\ C_{13} & C_{13} & C_{33} & 0 & 0 & 0 \\ 0 & 0 & 0 & C_{44} & 0 & 0 \\ 0 & 0 & 0 & 0 & C_{44} & 0 \\ 0 & 0 & 0 & 0 & 0 & C_{66} \end{pmatrix}$
Triclinic	21	$C = \begin{pmatrix} C_{11} & C_{12} & C_{13} & C_{14} & C_{15} & C_{16} \\ C_{12} & C_{22} & C_{23} & C_{24} & C_{25} & C_{26} \\ C_{13} & C_{23} & C_{33} & C_{34} & C_{35} & C_{36} \\ C_{14} & C_{24} & C_{34} & C_{44} & C_{45} & C_{46} \\ C_{15} & C_{25} & C_{35} & C_{45} & C_{55} & C_{56} \\ C_{16} & C_{26} & C_{36} & C_{46} & C_{56} & C_{66} \end{pmatrix}$

Table 9: Number of independent components in the elastic tensor for different crystal systems.

Crystal system	point groups	Number of independent elements	Piezoelectric tensor
Trigonal	32	2	$\mathbf{e} = \begin{pmatrix} \mathbf{e}_{11} & -\mathbf{e}_{11} & 0 & \mathbf{e}_{14} & 0 & 0 \\ 0 & 0 & 0 & 0 & -\mathbf{e}_{14} & -\mathbf{e}_{11} \\ 0 & 0 & 0 & 0 & 0 & 0 \end{pmatrix}$
Monoclinic	2	8	$\mathbf{e} = \begin{pmatrix} 0 & 0 & 0 & \mathbf{e}_{14} & 0 & \mathbf{e}_{16} \\ \mathbf{e}_{21} & \mathbf{e}_{22} & \mathbf{e}_{23} & 0 & \mathbf{e}_{25} & 0 \\ 0 & 0 & 0 & \mathbf{e}_{34} & 0 & \mathbf{e}_{36} \end{pmatrix}$
Triclinic	1	18	$\mathbf{e} = \begin{pmatrix} \mathbf{e}_{11} & \mathbf{e}_{12} & \mathbf{e}_{13} & \mathbf{e}_{14} & \mathbf{e}_{15} & \mathbf{e}_{16} \\ \mathbf{e}_{21} & \mathbf{e}_{22} & \mathbf{e}_{23} & \mathbf{e}_{24} & \mathbf{e}_{25} & \mathbf{e}_{26} \\ \mathbf{e}_{31} & \mathbf{e}_{32} & \mathbf{e}_{33} & \mathbf{e}_{34} & \mathbf{e}_{35} & \mathbf{e}_{36} \end{pmatrix}$

Table 10: Number of independent components in the piezoelectric tensor for different crystal systems.

the piezoelectric tensor dataset, the piezoelectric tensor is represented using Voigt notation as a 3×6 matrix, rather than a $3 \times 3 \times 3$ third-order tensor (see Appendix A.9 for details). we only predict the 3×6 matrix. In the elastic tensor dataset, the elastic tensor is represented using Voigt notation as a 6×6 symmetric matrix, rather than a $3 \times 3 \times 3 \times 3$ fourth-order tensor [14, 46]. Therefore, we predict the 6×6 matrix during usage (see Appendix A.9 for details).

Experimental Settings. The experiments were performed using a single NVIDIA GeForce RTX 3090 GPU. For benchmarking, we directly utilized the codebases for MEGNET, ETGNN, and GMTNet as provided by Yan et al. [51]. For each property, the dataset is split into training, validation, and test sets in an 8:1:1 ratio. During model training, Huber loss, AdamW [24], a weight decay of 10^{-5} , and polynomial learning rate decay were employed.

Dataset	Sample size	Fnorm Mean	Fnorm STD	Unit
Dielectric	4713	14.7	18.2	Unitless
Piezoelectric	4998	0.43	3.09	C/m ²
Elastic	25110	306.4	238.4	GPa

Table 11: Dataset statistics.

Hyperparameter settings of GoeCTP. When constructing the crystal graph, we used the 16th nearest atom to determine the cutoff radius. For edge embeddings, we used an RBF kernel with $c = 0.75$ and values ranging from -4 to 0 , which maps $-c/||\mathbf{e}_{ij}||_2$ to a 512-dimensional vector. In the dielectric and piezoelectric tensor prediction task, the 512-dimensional vector is mapped to a 128-dimensional vector through a non-linear layer, while in the elastic tensor prediction, it is mapped to a 256-dimensional vector. For the prediction module, eComFormer, in the dielectric and piezoelectric tensor prediction task, we used 4 node-wise transformer layers and 1 node-wise equivariant updating layer, whereas in the elastic tensor prediction, we used 2 node-wise transformer layers and 1 node-wise equivariant updating layer. For both dielectric, piezoelectric, and elastic tensor tasks, the learning rate was set to 0.001, with 200 epochs and a batch size of 64. In the Reverse R&R module, for the dielectric tensor prediction task, the 128-dimensional vector features output by the prediction module are mapped to a 6-dimensional vector through two non-linear layers, then reconstructed into a 3×3 matrix and combined with the orthogonal matrix \mathbf{Q} obtained from the R&R

	MEGNET	ETGNN	GMTNet	GoeCTP (eCom.)	GoeCTP (iCom.)	GoeCTP (Crys.)
Fnorm ↓	3.71	3.40	3.28	3.23	3.40	3.53
EwT 25% ↑	75.8%	82.6%	83.3%	83.2%	81.7%	80.1%
EwT 10% ↑	38.9%	49.1%	56.0%	56.8%	53.8%	52.9%
EwT 5% ↑	18.0%	25.3%	30.5%	35.5%	32.3%	30.6%
Total Time (s) ↓	663	1325	1611	616	535	645
Time/batch (s) ↓	0.052	0.104	0.126	0.048	0.042	0.202

Table 12: Additional comparison of performance metrics on dielectric dataset.

	MEGNET	ETGNN	GMTNet	GoeCTP (eCom.)	GoeCTP (iCom.)	GoeCTP (Crys.)
Fnorm ↓	0.504	0.515	0.450	0.431	0.448	0.457
EwT 25% ↑	39.3%	36.3%	45.5%	46.9%	45.5%	42.7%
EwT 10% ↑	27.1%	20.5%	38.1%	42.9%	44.9%	42.1%
EwT 5% ↑	11.4%	13.0%	34.3%	39.7%	38.3%	41.5%
Total Time (s) ↓	943	1220	5771	938	909	2787
Time/batch (s) ↓	0.074	0.095	0.45	0.073	0.071	0.218

Table 13: Additional comparison of performance metrics on piezoelectric dataset.

	MEGNET	ETGNN	GMTNet	GoeCTP (eCom.)	GoeCTP (iCom.)	GoeCTP (Crys.)
Fnorm ↓	143.86	123.64	117.62	107.11	102.80	107.44
EwT 25% ↑	23.6%	32.0%	36.0%	42.5%	46.7%	43.5%
EwT 10% ↑	3.0%	3.8%	7.6%	15.3%	18.6%	15.8%
EwT 5% ↑	0.5%	0.5%	2.0%	7.2%	8.2%	7.9%
Total Time (s) ↓	2899	4448	> 36000	2422	4035	7891
Time/batch (s) ↓	0.226	0.348	> 2.813	0.189	0.315	0.616

Table 14: Additional comparison of performance metrics on elastic dataset.

module to achieve $O(3)$ equivariant output. For the piezoelectric prediction task, the 18-dimensional vector features output by the prediction module are reconstructed into a 3×6 matrix and combined with the orthogonal matrix \mathbf{Q} from the R&R module to achieve $O(3)$ equivariant output. For the elastic tensor prediction task, the 256-dimensional vector features output by the prediction module are mapped to a 36-dimensional vector through two non-linear layers, then reconstructed into a 6×6 matrix and combined with the orthogonal matrix \mathbf{Q} from the R&R module to achieve $O(3)$ equivariant output.

Hyperparameter settings of GMTNet, ETGNN, and MEGNET. Following Yan et al. [51], we trained GMTNet, ETGNN, and MEGNET for 200 epochs using Huber loss with a learning rate of 0.001 and Adam optimizer with 10^{-5} weight decay across all tasks. The same polynomial learning rate decay scheduler is used in all experiments.

A.11 Additional results.

We assessed the performance of GoeCTP when combined with iComFormer [50] and CrystalFormer [42] (denoted as GoeCTP (iCom.) for the combination) on both the dielectric, piezoelectric, and elastic tensor datasets. As presented in Table 12, on the dielectric tensor dataset, although the prediction accuracy of GoeCTP (iCom.) and GoeCTP (Crys.) did not exceed that of GoeCTP (eCom.), GoeCTP (iCom.) demonstrated slightly higher computational efficiency compared to GoeCTP (eCom.). As shown in Table 13, similar to the dielectric tensor dataset, GoeCTP (eCom.) achieved the best prediction accuracy on the piezoelectric dataset, but GoeCTP (iCom.) demonstrated slightly higher computational efficiency compared to GoeCTP (eCom.). In contrast, as shown in Table 14, on the elastic tensor dataset, GoeCTP (iCom.) and GoeCTP (Crys.) achieved superior prediction quality relative to GoeCTP (eCom.), albeit with lower efficiency.

A.12 The limitations of our method and its broader impact

Limitations. (1) As discussed in the main text, GoeCTP is a plug-and-play $O(3)$ -equivariant framework designed to enhance the backbone network’s ability to achieve equivariant predictions. Conse-

quently, the performance of our method is inherently dependent on the capabilities of the backbone network. If the backbone lacks sufficient predictive power, the combined framework may not fully surpass the state-of-the-art tensor prediction networks in all evaluation metrics. For instance, as shown in Table 12, when our framework is integrated with CrystalFormer [42], although the computational speed significantly exceeds that of GMTNet, the Fnorm, EwT 25%, and EwT 10% values are lower than those achieved by GMTNet.

(2) As demonstrated in Higham [12] and Proposition 3.5, polar decomposition applied to a 3×3 invertible matrix \mathbf{L} produces a unique 3×3 orthogonal matrix \mathbf{Q} . For 3D crystal structures, the lattice matrix \mathbf{L} is always full-rank (i.e. invertible), therefore, ensuring the applicability of our method to 3D crystal systems. However, for certain special cases, such as 2D crystals with single-layer structures [32, 39], the rank of the lattice matrix \mathbf{L} may be less than 3. In these scenarios, directly applying polar decomposition may not yield a unique 3×3 orthogonal matrix \mathbf{Q} and a unique canonical form \mathbf{H} . This limitation could cause our method to fail, as crystals with different spatial orientations cannot be consistently adjusted to a unique canonical form, thereby preventing the method from achieving the desired $O(3)$ -equivariance.

Broader impact. This work can be applied to screen existing crystal material databases for potential material candidates, facilitating the discovery of new materials with desirable tensor properties, such as high-dielectric materials. Therefore, our work has the potential to make a significant impact on materials science.

A.13 How to further utilize the tensor properties symmetry

In this section, we will use the dielectric tensor as an example to briefly discuss how to further utilize the symmetry of tensor properties.

Utilizing symmetry constraints for zero elements. To demonstrate the role of symmetry constraints, we present an example of the GoeCTP prediction results in Table 15. Within a reasonable margin of error, the predictions align well with the expected constraints.

Label	Prediction	Cubic dielectric tensor
$\begin{pmatrix} 2.258 & 0 & 0 \\ 0 & 2.258 & 0 \\ 0 & 0 & 2.258 \end{pmatrix}$	$\begin{pmatrix} 2.252 & 0.016 & 0.008 \\ 0.016 & 2.230 & 0.007 \\ 0.008 & 0.007 & 2.262 \end{pmatrix}$	$\varepsilon = \begin{pmatrix} \varepsilon_{11} & 0 & 0 \\ 0 & \varepsilon_{11} & 0 \\ 0 & 0 & \varepsilon_{11} \end{pmatrix}$

Table 15: An example of GoeCTP prediction results

Crystal system	Cubic	Tetragonal	Hexagonal-Trigonal	Orthorhombic	Monoclinic
Success rate	88.3%	86.6%	84.5%	84.5%	75.7%

Table 16: The GoeCTP results of predicting symmetry-constrained zero-valued dielectric tensor elements.

For a dielectric tensor, we evaluate the prediction of zero elements by defining a threshold as 1% of the average value of non-zero elements in the labels. Predictions are deemed successful if they meet this threshold. The results are as shown in Table 16. It can be observed that our method predicts most zero elements accurately, though not flawlessly. Since our advantage lies in transferring equivariance through an external framework, there are no restrictions on the model itself. Therefore, to achieve a higher success rate for zero elements, we added a ReLU activation function to the output layer of the network to improve the success rate (this applies only to cases where tensor elements are greater than or equal to zero). The results after retraining GoeCTP are as shown in Table 17, Table 18, and Table 19. Our method predicts zero elements more accurately while maintaining overall performance.

This simple modification enables GoeCTP to more accurately predict the zero elements in dielectric tensors caused by the space group constraints.

Utilizing symmetry constraints for non-zero elements. The symmetry constraints for zero elements serve as a foundational example. When the space group of the input crystal is known, prior knowledge (refer to Appendix A.9) can be employed to ensure that network outputs fully adhere to tensor property constraints. There are two specific methods to achieve this.

Label	Prediction	Cubic dielectric tensor
$\begin{pmatrix} 2.258 & 0 & 0 \\ 0 & 2.258 & 0 \\ 0 & 0 & 2.258 \end{pmatrix}$	$\begin{pmatrix} 2.237 & 0.000 & 0.000 \\ 0.000 & 2.283 & 0.000 \\ 0.000 & 0.000 & 2.228 \end{pmatrix}$	$\varepsilon = \begin{pmatrix} \varepsilon_{11} & 0 & 0 \\ 0 & \varepsilon_{11} & 0 \\ 0 & 0 & \varepsilon_{11} \end{pmatrix}$

Table 17: An example of GoeCTP (ReLU) prediction results

Crystal system	Cubic	Tetragonal	Hexagonal-Trigonal	Orthorhombic	Monoclinic
Success rate	100%	100%	87.2%	100%	100%

Table 18: The GoeCTP (ReLU) results of predicting symmetry-constrained zero-valued dielectric tensor elements.

	GoeCTP	GoeCTP (ReLU)
Fnorm ↓	3.23	3.26
EwT 25% ↑	83.2%	82.6%
EwT 10% ↑	56.8%	58.4%
EwT 5% ↑	35.5%	36.3%

Table 19: Performance comparisons between GoeCTP and GoeCTP (ReLU) on the dielectric dataset.

In the first method, only the independent components of the tensor properties are predicted. For example, for a cubic crystal, we predict only one independent component and then use the mask from Table 8 to reconstruct it into a 3×3 tensor). In Table 15, GoeCTP was modified to directly predict independent components. The new results are shown in Table 20, which fully satisfy the symmetry constraints. As shown in Table 21, the overall prediction performance indicates that directly predicting the independent components improves the model’s Fnorm performance on the dielectric dataset. Since this method directly predicts independent components, it is more suitable for cases like the dielectric tensor, where the independent components exhibit relatively simple structures. However, for more complex datasets, such as those involving piezoelectric and elastic tensors, the model’s performance using this method may degrade. In such scenarios, the second method provides a more viable alternative.

Label	Prediction	Cubic dielectric tensor
$\begin{pmatrix} 2.258 & 0 & 0 \\ 0 & 2.258 & 0 \\ 0 & 0 & 2.258 \end{pmatrix}$	$\begin{pmatrix} 2.357 & 0.000 & 0.000 \\ 0.000 & 2.357 & 0.000 \\ 0.000 & 0.000 & 2.357 \end{pmatrix}$	$\varepsilon = \begin{pmatrix} \varepsilon_{11} & 0 & 0 \\ 0 & \varepsilon_{11} & 0 \\ 0 & 0 & \varepsilon_{11} \end{pmatrix}$

Table 20: An example of GoeCTP (predicting the independent components) prediction results

	GoeCTP	GoeCTP (independent)
Fnorm ↓	3.23	3.11
EwT 25% ↑	83.2%	80.5%
EwT 10% ↑	56.8%	57.3%
EwT 5% ↑	35.5%	35.5%

Table 21: Performance comparisons between GoeCTP and GoeCTP (predicting the independent components) on the dielectric dataset.

In the second method, once the network training is completed, the network output is weighted using the standard tensor property format, referred to as a mask, as detailed in Table 8. The application of this method to the piezoelectric and elastic datasets is demonstrated in Tables 22 and 23. The results indicate that incorporating symmetry-based weighting effectively improves the performance of GoeCTP.

	GoeCTP	GoeCTP (weighted)
Fnorm ↓	0.431	0.389
EwT 25% ↑	46.9%	48.5%
EwT 10% ↑	42.9%	46.7%
EwT 5% ↑	39.7%	46.1%

Table 22: Performance comparisons between GoeCTP and GoeCTP (weighted by the standard tensor property form) on the piezoelectric dataset.

	GoeCTP	GoeCTP (weighted)
Fnorm ↓	107.11	106.24
EwT 25% ↑	42.5%	46.3%
EwT 10% ↑	15.3%	16.5%
EwT 5% ↑	7.2%	7.4%

Table 23: Performance comparisons between GoeCTP and GoeCTP (weighted by the standard tensor property form) on the elastic dataset.

A.14 Analysis of discontinuity in canonicalization

Previous studies [6] have shown that canonicalization can often introduce discontinuities into the model. To assess the impact of such discontinuities on our method, we analyze our proposed method from both theoretical and empirical perspectives.

From theoretical perspective: The following proposition, presented in Appendix B of Dym et al. [6], characterizes the existence of a continuous canonicalization under orthogonal group actions:

Proposition A.3. *Consider the action of the orthogonal group $O(d)$ on $\mathbf{X} \in \mathbb{R}^{n \times d}$. There exists a continuous canonicalization for $O(d)$ when $n \leq d$. This continuous canonicalization can be defined as $y_{\mathbf{X}} = (\mathbf{X}^\top \mathbf{X})^{1/2}$, where $\mathbf{X}^\top \mathbf{X}$ forms a positive semi-definite matrix and the square root is the standard square root of a positive semi-definite matrix, i.e. $(\mathbf{A})^{1/2}$ is the unique positive semidefinite matrix \mathbf{B} such that $\mathbf{B}^2 = \mathbf{A}$.*

In fact, the polar decomposition adopted in this work can be regarded as a case of such continuous canonicalization.

Proof. According to Proposition A.3, for a matrix $\mathbf{L} \in \mathbb{R}^{3 \times 3}$, its continuous canonicalization norm is given by $y_{\mathbf{L}} = (\mathbf{L}^\top \mathbf{L})^{1/2}$.

In this work, the polar decomposition is applied to the lattice matrix $\mathbf{L} = \mathbf{QH}$, $\mathbf{L} \in \mathbb{R}^{3 \times 3}$, where \mathbf{Q} is an orthogonal matrix, and \mathbf{H} is the positive semi-definite Gram matrix (which serves as the canonicalization norm). Based on the properties of positive semi-definite matrices, our method is actually equivalent to the canonicalization approach described in Proposition A.3, i.e. $y_{\mathbf{L}} = (\mathbf{L}^\top \mathbf{L})^{1/2} = ((\mathbf{QH})^\top \mathbf{QH})^{1/2} = (\mathbf{H}^\top \mathbf{H})^{1/2} = \mathbf{H}$. \square

Therefore, our canonicalization via polar decomposition is consistent with the continuous canonicalization.

From empirical perspective: To further demonstrate how this discontinuity affects the accuracy of tensor property predictions, we conducted a set of comparative experiments in which we replaced the polar decomposition in GoeCTP with QR decomposition [22] for evaluation. In this QR decomposition case, the lattice matrix is decomposed as $\mathbf{L} = \mathbf{QR}$, where \mathbf{Q} is an orthogonal matrix, and \mathbf{R} is an upper triangular matrix that serves as the canonicalization norm. However, \mathbf{R} does not satisfy Proposition A.3, and therefore does not constitute a continuous canonicalization approach.

To assess the sensitivity of each approach to small structural perturbations, we used the crystal CdI_2 (JARVIS_ID: JVASP-29631) as the model input, and then perturbed its lattice matrix (specifically, scaling down the first row of the lattice matrix) to observe the relative changes in the output

(specifically the variations in the Fabenius norm of the output tensor). The detailed results are as follows:

Perturbation Ratio	0%	5%	10%	15%	20%	25%	30%	35%	40%
Output variation ratio (%): GoeCTP (QR)	0	3.38	6.63	11.29	21.83	39.37	67.81	124.79	191.28
Output variation ratio (%): GoeCTP (polar)	0	2.53	1.23	2.03	4.84	12.72	24.88	36.34	45.67

Table 24: Output variation ratio under different perturbation ratios on the dielectric dataset

The results clearly show that the output of GoeCTP using polar decomposition exhibits significantly smaller relative changes compared to the QR-based variant, particularly under increasing levels of perturbation. This highlights the robustness of the continuous canonicalization afforded by polar decomposition, demonstrating its superiority in maintaining prediction stability and structural consistency under small input variations.

A.15 How to design other canonical forms

In fact, the canonical form obtained via polar decomposition provides a foundation from which infinitely many alternative canonical forms can be derived. Specifically, given a crystal with lattice matrix \mathbf{L} , polar decomposition yields $\mathbf{L} = \mathbf{QH}$. While \mathbf{H} serves as one valid canonical representation, additional canonical forms can be constructed by applying orthogonal transformations to \mathbf{H} . For instance, given a fixed orthogonal matrix \mathbf{Q}_0 (which may be arbitrarily chosen) or a neural network $f_Q(\mathbf{H}) = \mathbf{Q}_\theta$ that predicts an orthogonal matrix \mathbf{Q}_θ , one can construct new canonical forms such as $\mathbf{Q}_0\mathbf{H}$ or $\mathbf{Q}_\theta\mathbf{H}$. This is because, for any given crystal with an arbitrary orientation, a fixed canonical form can be obtained according to a predefined computation rule, i.e. $\mathbf{L} = \mathbf{QH} \rightarrow \mathbf{L} = \mathbf{QQ}_0^\top \mathbf{Q}_0\mathbf{H}$ or $\mathbf{L} = \mathbf{QQ}_\theta^\top \mathbf{Q}_\theta\mathbf{H}$. This formulation highlights the inherent flexibility in defining canonical forms.

A.16 Impact of different canonical form on tensor property prediction

As discussed in Appendix A.15, there exist infinitely many possible canonical forms. To investigate the impact of different canonical forms on tensor property prediction in crystalline materials, we first present the results comparing the performance of GoeCTP with QR decomposition [22] and GoeCTP without canonicalization. The corresponding results are summarized in the table below:

	GoeCTP (QR)	GoeCTP (polar)	GoeCTP (w/o QR or polar)
Fnorm ↓	3.20	3.23	3.60
EwT 25% ↑	83.5%	83.2%	80.6%
EwT 10% ↑	56.0%	56.8%	56.2%
EwT 5% ↑	32.4%	35.5%	32.6%
Total Time (s) ↓	639	616	613

Table 25: Predictive performance comparisons between GoeCTP (QR), GoeCTP (polar), and GoeCTP (w/o QR or polar) on the dielectric dataset.

According to the results, it is evident that incorporating a canonical form improves tensor prediction performance compared to omitting it. While different canonical forms lead to slight variations in performance, the overall impact remains relatively modest. One possible explanation is that canonical forms typically exhibit structured representations, such as the symmetric positive semi-definite matrix obtained via polar decomposition or the upper triangular matrix from QR decomposition, which may facilitate the model’s ability to capture relevant features.

Furthermore, the use of a canonical form aligns all atoms within a crystal structure to a unified global coordinate system, thereby enabling equivariant tensor prediction. However, recent studies [43, 23, 15] have demonstrated that employing adaptive local frames, i.e. constructed based on individual atomic environments, can further enhance the accuracy of property predictions. Motivated by these insights, we extend the GoeCTP framework by incorporating local frames [43] (also referred to as local canonicalization). It is important to emphasize that GoeCTP can be seamlessly integrated

with any prediction network, including those based on local frames, while preserving its equivariant prediction capability. The corresponding results are presented below.

	GoeCTP (local frame+polar)	GoeCTP (polar)
Fnorm ↓	3.11	3.23
EwT 25% ↑	83.9%	83.2%
EwT 10% ↑	58.4%	56.8%
EwT 5% ↑	33.5%	35.5%
Total Time (s) ↓	1979	616

Table 26: Predictive performance comparisons between GoeCTP (local frame+polar) and GoeCTP (polar) on the dielectric dataset.

The results indicate that incorporating local frames can enhance predictive performance. However, this improvement comes at the expense of increased computational cost.